Research Square

Preprints are preliminary reports that have not undergone peer review.
They should not be considered conclusive, used to inform clinical practice,
or referenced by the media as validated information.

Development of Potential CDK9 Inhibitors through Pharmacophore-Based Virtual Screening, 3D-QSAR, Molecular Docking, MD Simulation, and In Vitro Anticancer Evaluation

Rajkumar Reddy Rajula

rajkumar.rajula@woxsen.edu.in

Woxsen University

Umadevi Etikyala

Osmania University

Dinesha P

National Institute of Technology Karnataka

Sampat P V

National Institute of Technology Karnataka

Shreeganesh Subraya Hedge

Dayananda Sagar University

Muzaffar-Ur-Rehman Mohammed

Birla Institute of Technology and Science, Pilani

Chandra Sekhar Kondapalli Venkata Gowri

Birla Institute of Technology and Science - Hyderabad Campus

Udayakumar Dalimba

National Institute of Technology Karnataka

Vijjulatha Manga

Osmania University

Article

Keywords: Pharmacophore-Based Virtual Screening, 3D-QSAR, Molecular Docking, Binding Free Energy and Anticancer activity

Posted Date: March 24th, 2026

DOI: https://doi.org/10.21203/rs.3.rs-9086560/v1

License: This work is licensed under a Creative Commons Attribution 4.0 International License.
Read Full License

Additional Declarations: No competing interests reported.

Version of Record: A version of this preprint was published at Scientific Reports on April 28th, 2026. See the published version at https://doi.org/10.1038/s41598-026-50502-5.

Development of Potential CDK9 Inhibitors through Pharmacophore-Based Virtual Screening, 3D-QSAR, Molecular Docking, MD Simulation, and *In Vitro* Anticancer Evaluation

Rajkumar Reddyrajula[a,*], Umadevi Etikyala[b], Dinesha P[c], Sampat P V[c], Shreeganesh Subraya Hedge[c,d], Mohammed Muzaffar-Ur-Rehman[e], Chandra Sekhar Kondapalli Venkata Gowri[f], Udayakumar Dalimba[c], Vijjulatha Manga[b,*]

[a]*Department of Chemistry, School of Sciences, Woxsen University, Hyderabad -502345, Telangana, India.*

[b]*Medicinal Chemistry Laboratory, Department of Chemistry, Osmania University, Hyderabad-500 076, Telangana, India.*

[c]*Department of Chemistry, National Institute of Technology Karnataka, Surathkal-575025, Mangalore, Karnataka, India.*

[d]*Department of Chemistry, School of Engineering, Dayananda Sagar University, Harohalli, Bengaluru -562112, Karnataka, India.*

[e]*Medicinal Chemistry Research Laboratory, Department of Pharmacy, Birla Institute of Technology and Science Pilani, Pilani Campus, Pilani-333031, Rajasthan. India.*

[f]*Department of Chemistry, Birla Institute of Technology and Science Pilani, Hyderabad Campus, Jawahar Nagar, Kapra Mandal, Hyderabad 500078, Telangana, India.*

*** Corresponding authors -** rajkumar.reddyrajula111@gmail.com, Vijjulathamanga@gmail.com

Abstract

Cyclin-dependent kinase 9 (CDK9) is a transcription-regulating serine/threonine kinase, and the dysregulation drives tumour initiation, thereby establishing CDK9 inhibition as a mechanistically validated and therapeutically attractive strategy for the treatment of diverse malignancies. In this study, a comprehensive computational strategy was utilized to identify novel CDK9 inhibitors. A pharmacophore-based virtual screening was implemented in combination with atom-based 3D-QSAR, molecular docking, binding free energies, *in silico* ADME, and MD simulation studies. A statistically validated five-point pharmacophore model (ADHRR) was developed and demonstrated strong predictive performance (R^2 = 0.98, Q^2 = 0.84). This optimized model was used to screen chemical databases for potential CDK9 inhibitors. Structural insights gained from the resulting hits guided the rational design of indole-based biphenyl amide hybrids (IBA's). Seven analogues (**D1**-**D7**) exhibited strong binding affinities comparable to or greater than those of the screened hits and the reference CDK9 inhibitor **23**. Additionally, molecular dynamics simulations and DFT analysis confirmed the stability of both **D3** and **D6** complexes. Subsequent synthesis and biological evaluation against a panel of cancer cell lines identified compounds **D3** and **D6** as the most potent.

Collectively, these results identify **D3** and **D6** as promising lead candidates for further CDK9-focused medicinal chemistry optimization and mechanistic studies.

Key words: Pharmacophore-Based Virtual Screening, 3D- QSAR, Molecular Docking, Binding Free Energy and Anticancer activity.

1. Introduction

Cyclin-dependent kinases (CDKs) represent a highly conserved family of serine/threonine kinases, and their catalytic activity is precisely regulated by cyclin binding, jointly responsible for various fundamental cellular processes.[1] Based on function, CDKs are broadly divided into two types: i) cell-cycle regulators (CDK1, CDK2, CDK4, and CDK6) and ii) transcription-associated kinases (CDK7, CDK8, and CDK9). Abnormal regulation of cell-cycle CDKs is a well-established hallmark of tumorigenesis, increasing evidence highlights transcriptional CDKs, particularly CDK9, as playing a crucial role in driving oncogenic transcriptional programs.[2,3] Acting as the catalytic core of the positive transcription elongation factor b (P-TEFb) complex, CDK9 phosphorylates the Ser2 residue within the heptapeptide repeats (YSPTSPS) of the RNA polymerase II carboxy-terminal domain, thereby releasing promoter-proximal paused polymerase into productive elongation. Abnormal activation of CDK9 sustains transcription of short-lived, anti-apoptotic proteins such as myeloid cell leukemia-1 (MCL-1), promoting malignant transformation and tumor cell survival. Consequently, pharmacological inhibition of CDK9 results in rapid MCL-1 depletion and suppression of tumor growth, establishing CDK9 as a compelling therapeutic target in cancer and other diseases, including HIV infection.[4–7] Early pan-CDK inhibitors, such as flavopiridol and dinaciclib, demonstrated potent CDK9 inhibition with robust antitumor activity but were hindered by limited selectivity and dose-limiting toxicities, complicating clinical translation (**Figure 1**). These efforts yielded additional nonselective inhibitors, including AT7519, roniciclib, R547, and BMS-387032, some of which advanced into late-stage clinical evaluation. However, these limitations spurred the rational design of selective CDK9 inhibitors, which validated transcriptional repression as a viable therapeutic strategy.[8] It is worth highlighting that preclinical agents such as the amidopyridine-based AZ5576 induced rapid loss of RNAPII Ser2 phosphorylation, profound MCL-1 suppression, and caspase-dependent apoptosis in hematological malignancies, translating into significant antitumor efficacy *in vivo* (**Figure 2**). Further optimization led to additional selective scaffolds, including LDC000067 and LY2857785, reinforcing CDK9 as a druggable transcriptional node. Importantly, the recent clinical progression of selective CDK9 inhibitors, such as NVP-2, BAY

1143572 and BAY 1251152, represents a major milestone in CDK9-targeted drug discovery.[9,10] Nevertheless, challenges related to selectivity, toxicity, and therapeutic window persist, underscoring the urgent need for continued discovery and development of next-generation CDK9 inhibitors with improved pharmacological profiles.

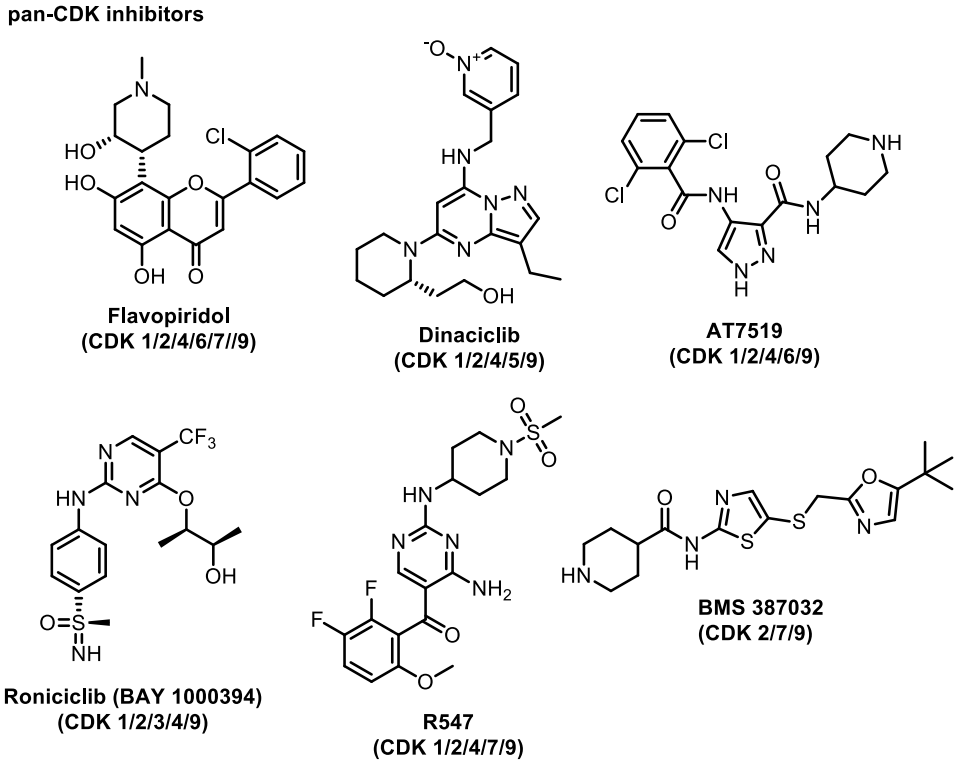


Figure 1. Chemical structures of pan-CDK inhibitors.

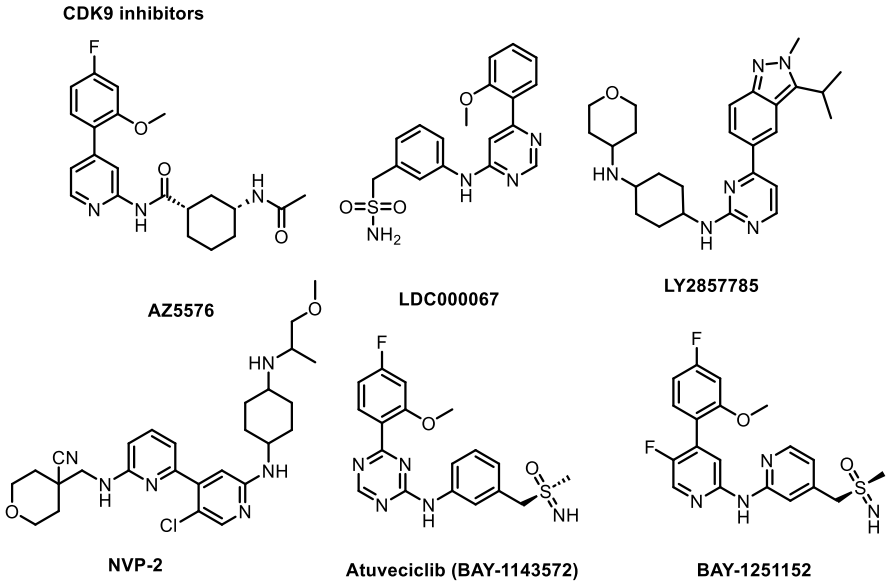


Figure 2. Chemical structures of CDK9 inhibitors.

Recent advances in CDK9-targeted drug discovery demonstrate that the integrating modern in silico methodologies with experimental validation markedly enhanced the efficient

identification of potent and selective CDK9 inhibitors.[11–15] For example, Hirokawa *et al.* combined molecular dynamics simulations, cheminformatics-based screening, and structure-based docking to uncover compounds I and II (**Figure 3**) that exploit a cryptic allosteric cavity encompassing the CCII and CCIII regions of CDK9; these ligands were experimentally validated and demonstrated additive inhibitory effects when co-administered with the ATP-competitive inhibitor BS-181.[16] Complementarily, large-scale docking followed by extended 500 ns molecular dynamics simulations of a natural product library identified FL_72 (III) and PH_435 (IV) as selective CDK9 inhibitors, supported by stable conformational dynamics, favourable binding free energies, and persistent interactions with key catalytic residues.[17] In a data-driven approach, Dong *et al.* employed a hybrid virtual screening strategy integrating machine learning based prediction with structure-based docking, leading to the discovery of a novel CDK9 inhibitor for acute myeloid leukaemia, exemplified by compound V with nanomolar potency (IC_{50} = 31.28 nM) and robust antiproliferative activity in hematologic tumor cell lines.[18] Additional structure-based workflows revealed that ligand 006 (VI) undergoes adaptive conformational rearrangement within the CDK9 binding pocket, enabling sustained hydrogen-bonding interactions with the catalytic Asp109 residue.[19] Likewise, computer-assisted drug design approaches combining predictive QSAR modelling with *in silico* synthesis identified compounds T1 (VII) and T2 (VIII) as promising CDK9 inhibitors, exhibiting enhanced binding affinity, dynamic stability, and favorable ADMET profiles relative to reference ligands.[20] Integrated multiscale *in silico* pipelines encompassing virtual screening, molecular docking, molecular dynamic simulations, 3D-QSAR modelling, MM/PBSA free energy calculations, and ADME assessment further identified compound IX with 71% inhibitory activity against CDK9.[21] Finally, a comprehensive computational framework incorporating 3D-QSAR, fingerprint analysis, docking, molecular dynamic simulations, MMGB/PBSA calculations, and ADMET evaluation highlighted compound D98 (X) as a high-affinity CDK9 inhibitor stabilized by critical interactions with Ala153 and possessing a pharmacokinetic profile indicative of strong *in vivo* translational potential.[22] Taken together, these studies establish pharmacophore-based and 3D-QSAR driven strategies, particularly when coupled with molecular docking and rigorous free energy analyses, as indispensable tools for the rational design of next-generation CDK9 inhibitors. Given this background, we developed a new series of structurally novel CDK9 inhibitors employing an integrated computational framework encompassing atom-based 3D-QSAR analysis, pharmacophore-based virtual screening, molecular docking, prime MM/GBSA binding free

energy calculation, and *in silico* ADME profiling. The top-ranked hits were identified and the emerging from this workflow were successfully synthesized and experimentally evaluated against a panel of human cancer cell lines to validate their antiproliferative efficacy and translational potential.

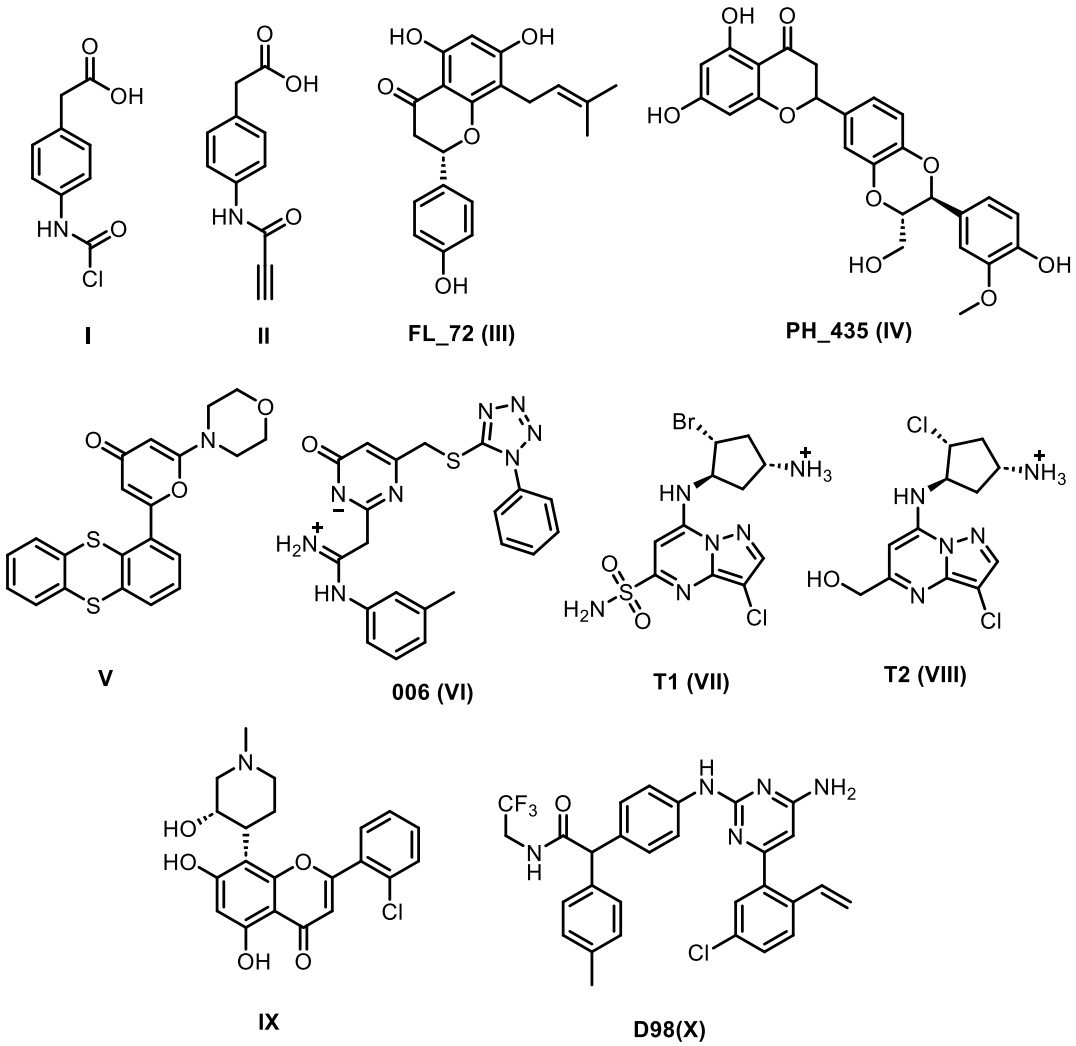


Figure 3. Recently reported CDK9 inhibitors *via in silico* techniques.

2. Materials and methods

2.1 Dataset

To generate a statistically robust pharmacophore model, a dataset of 55 structurally diverse small-molecule CDK9 inhibitors was compiled from the literature, encompassing a wide activity range with pIC_{50} values between 7.06 and 10.40.[23–25] The dataset was rationally divided into training and test sets based on activity distribution and key physicochemical attributes to ensure balanced representation of chemical space. The training set was employed for pharmacophore hypothesis generation and 3D-QSAR model construction, whereas the test

set was reserved exclusively for internal validation. Compounds with $pIC_{50} > 8$ were designated as active, while those with $pIC_{50} \leq 8$ were classified as inactive to enable stringent feature discrimination. The pIC_{50} values, binding energies, and pharmacophore fitness scores of all compounds are summarized in **Tables S1-S4 (**Supplementary Information**)**.

2.2 Ligand preparation

Accurate three-dimensional ligand representations are essential for reliable pharmacophore model development. Owing to the conformational flexibility of the ligands, extensive sampling of thermodynamically accessible low-energy conformers was performed to capture potential bioactive geometries. All compounds were initially sketched in the Maestro build panel, converted to 3D structures, and prepared using the LigPrep module.[26] The resulting low-energy conformers, together with their activity annotations, were imported into the PHASE workflow. Ligands were classified as active or inactive using predefined activity thresholds to enable statistically meaningful pharmacophore hypothesis generation.

2.3 Pharmacophore model generation

Ligand pharmacophores are defined as spatial arrangements of key interaction features that mediate noncovalent recognition by the target receptor. To create pharmacophore hypotheses, PHASE utilizes six basic pharmacophoric features: hydrogen-bond donor (D), hydrogen-bond acceptor (A), hydrophobic group (H), aromatic ring (R), negative (N), and positive (P) ionizable centers. [27] Potential pharmacophoric sites are identified based on shared structural and interaction patterns across the ligand dataset and are mapped onto three-dimensional geometries. Ligand conformations exhibiting identical feature compositions and spatial arrangements are clustered into common pharmacophore models using a tree-based partitioning approach that evaluates inter-feature distances and geometric similarity.[28]

2.4 Scoring hypotheses

Pharmacophore scoring enables the identification of the most predictive hypothesis by quantitatively assessing how effectively active ligands map onto key interaction features. The generated hypotheses provide insight into the binding characteristics of active ligands at the receptor interface. PHASE scoring incorporates contributions from site-point and vector alignment, volumetric overlap, selectivity, number of matched ligands, and correlation with

biological activity. The best pharmacophore hypothesis was identified based on a combined score analysis and the mapping fidelity of active compounds.

2.5 Building a 3D-QSAR model

The 3D-QSAR models in PHASE were developed using the biological activity of ligands mapped to the selected pharmacophore hypothesis. Atom-based 3D-QSAR modelling was performed using PLS regression with binary spatial of descriptors, and model quality was assessed based on the alignment consistency of the training set ligands. Using the best five-point hypothesis, 3D-QSAR models for CDK9 inhibitors were constructed from 42 training set compounds with a grid spacing of 1.0 Å. Models incorporating one to three PLS factors were constructed and validated using both training and test sets.

2.6 Virtual screening

Virtual screening was employed to identify potential CDK9 inhibitors from large chemical databases. The best atom-based 3D-QSAR pharmacophore models were used as three-dimensional queries for screening, requiring a minimum match of four out of five pharmacophoric features. Application of the optimized ADHRR pharmacophore in PHASE enabled the identification of pharmacophore-matched compounds from the Zinc database comprising 11719 molecules with no reported CDK9 inhibitory activity.[29]

2.7 Molecular docking and binding free energy calculations

Molecular docking was performed to investigate the binding modes and interaction profiles of ligands within the CDK9 active site using the glide module of the Schrodinger software. The crystal structure of CDK9 (PDB ID: 4BCF) was retrieved from the RCSB Protein Data Bank and prepared using the Protein Preparation Wizard in Maestro, followed by restrained minimization with the OPLS-2005 force field. Receptor grids were generated in Glide using the co-crystallized ligand to define the binding site, with a grid size of 10 Å × 10 Å × 10 Å and van der Waals scaling of 0.9. Low-energy ligand conformers were docked using the XP protocol. Binding free energies of docked complexes were further evaluated using MM/GBSA calculations implemented in Prime.[30]

ΔG_{bind}bind was estimated by following equation

$$\Delta G_{bind} = E_{complex(minimized)} - \left[E_{ligand(unbound,minimized)} + E_{receptor(unbound,minimized)}\right]$$

2.8 *In silico* ADME prediction

ADME and drug-likeness properties are key determinants of lead viability and are among the major contributors to late-stage drug attrition.[31] In this study, *in silico* ADME profiling of hit compounds and newly designed molecules was performed using the QikProp module. Predicted parameters included octanol/water partition coefficient (QP logPo/w), aqueous solubility (QP log S), polar surface area (PSA), hydrogen-bond donor and acceptor counts, human serum albumin binding (QP log Khsa), Caco-2 cell permeability (QPP Caco), human oral absorption (%HOA), and blood-brain barrier partition coefficient (QP log BB) were computed.

2.9 MD Simulations

The docked complexes of the ligands D3 and D6 were used to determine the stability of binding by subjecting the complexes to molecular dynamics for a duration of 100 ns. The TPI3P solvent model was used to generate the boundary conditions of dimensions 10 Å3. Using an NPT ensemble class, the temperature was maintained at 310 K, and the constant pressure was 1.013 bar. The constant temperature and pressure for the entire simulation were maintained via the Nose-Hoover chain thermostat and Martyna-Tobias-Klein barostat respectively. Post MD simulations, the simulation interaction diagram was used to interpret the RMSD of the protein-ligand, followed by protein-ligand contacts, there by evaluating the stability of the protein-ligand complex.

3. Results and discussion

3.1 Determination of pharmacophore model

Three five-feature pharmacophore variants i.e ADHRR, AHRRR, and DHRRR comprising hydrogen-bond acceptor (A), hydrogen-bond donor (D), hydrophobic (H), and aromatic ring (R) features, were generated during common pharmacophore identification. Systematic evaluation of these variants resulted in the generation of 28 unique five-point pharmacophore hypotheses. The hypotheses were then ranked using PHASE survival scores, incorporating contributions from active and inactive ligand mapping, vector alignment, and volumetric overlap. Based on comprehensive score analysis and mapping consistency of active ligands, the five-point ADHRR pharmacophore hypothesis was selected for further investigation. The three-dimensional geometry of the optimized ADHRR model is illustrated in **Figure 4**, wherein

spheres A correspond to the hydrogen-bond acceptor feature, H indicates hydrophobic feature, D denotes the hydrogen-bond donor feature, and R represent aromatic ring interaction sites.

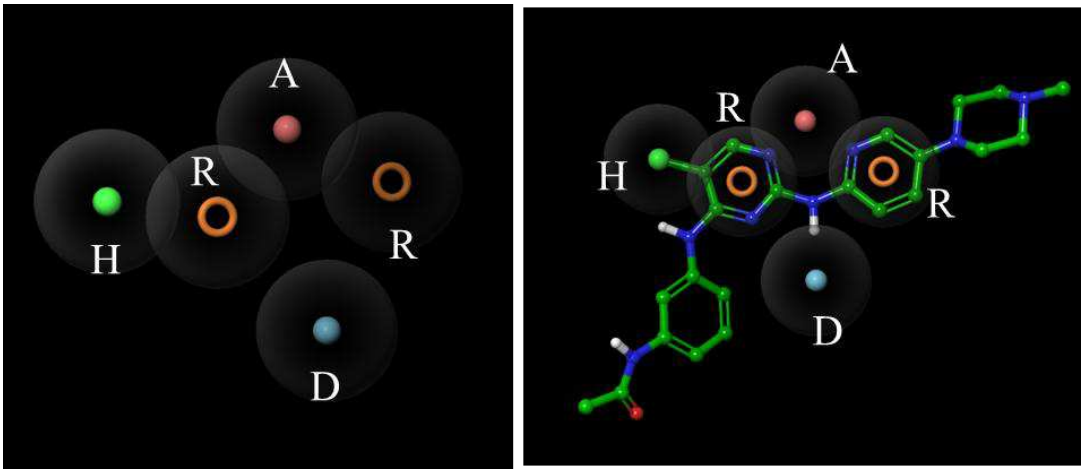


Figure 4. Obtained pharmacophore model ADHRR and representation with potent molecule **23**.

3.2 Validation of 3D-QSAR model

Table 1. The top three pharmacophore hypotheses through PHASE.

S.No	ID	SD	R^2	F	RMSE	Q^2	Pearson-R	Stability
1	**ADHRR**	**0.1442**	**0.9598**	**357.8**	**0.21**	**0.8435**	**0.9237**	**-0.0407**
2	AHRRR	0.2150	0.9188	226.3	0.24	0.5393	0.7459	-0.1
3	DHRRR	0.4442	0.6446	74.7	0.23	0.5775	0.8042	0.478

SD: Standard Deviation, **R^2:** coefficient of determination, **F:** variance ratio, **RMSE:** Root-Mean-Square Error, **Q^2:** robust internal predictivity, **Pearson-R:** Pearson correlation coefficient.

Atom-based 3D-QSAR models were developed for the top three pharmacophore hypotheses using partial least squares (PLS) regression analysis. In this approach, experimentally determined pIC_{50} values were employed as dependent variables, while the PHASE-derived atom-based descriptors and corresponding PLS factors served as independent variables. A comprehensive statistical summary of the resulting 3D-QSAR models for CDK9 inhibitors, based on both training and test set compounds, is presented in **Table 1**. Among the evaluated hypotheses, the ADHRR based 3D-QSAR model exhibited superior statistical performance, characterized by a high coefficient of determination ($R^2 = 0.96$), low standard deviation (SD = 0.14), a strong variance ratio (F = 357.8), robust internal predictivity ($Q^2 = 0.84$), low root-mean-square error (RMSE = 0.21), and a favorable Pearson correlation coefficient (R = 0.92). These statistical indices demonstrate the high predictive accuracy, robustness, and reliability of the developed model, underscoring its suitability for prospective lead optimization and

rational design efforts. The scatter plot illustrating the correlation between experimental and predicted pIC_{50} values for both training and test sets (**Figure 5**) reveals a strong positive linear relationship, further validating the statistical significance and predictive capability of the optimized 3D-QSAR model.

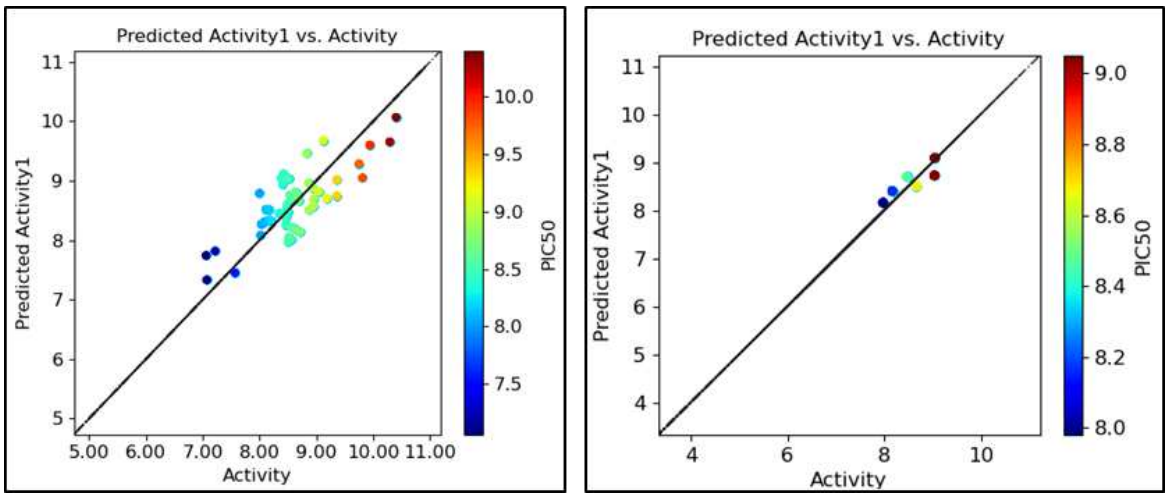


Figure 5. Scatter plot of experimental vs predicted pIC_{50} values.

3.3 3D-QSAR visualization of best active compound

Atom-based 3D-QSAR models emphasize steric compatibility between ligands and the receptor, whereas pharmacophore-based 3D-QSAR models predict activity based on the spatial distribution of key pharmacophoric features. Visualization of 3D-QSAR contour maps aids in elucidating structure-activity relationships. Figure 6 depicts the 3D-QSAR contour visualization of the most potent compound, molecule 23 (Expt. pIC_{50} = 10.40). In **Figure 6a**, blue contour cubes indicate regions favourable for hydrogen-bond donor interactions, whereas red cubes denote favourable hydrogen-bond acceptor regions, indicating contributions from the NH group as well as acceptor features associated with the pyridine and pyrimidine ring. In **Figure 6b**, blue cubes represent hydrophobic-favored regions, while red cubes denote hydrophobic-disfavored areas. Favourable hydrophobic contributions were observed in proximity to the aromatic benzene ring, and piperazine moieties, indicating that enhanced hydrophobic interactions at these positions are beneficial for CDK9 inhibitory activity. In conjunction, these observations suggest that the presence of additional hydrogen-bond donor, hydrogen-bond acceptor, and hydrophobic features beyond the core pharmacophore significantly enhances ligand potency, providing valuable guidance for further lead optimization.

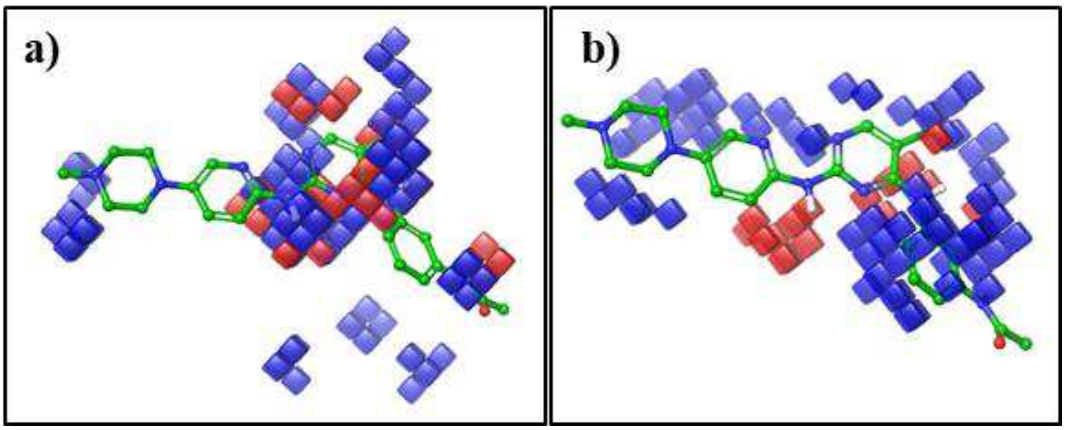


Figure 6. 3D-QSAR model visualization of the best active compound **23**, illustrating the effect of a) H-bond donor and H-bond acceptor features and b) hydrophobic features.

3.4 Pharmacophore-based virtual screening

Virtual screening represents a cornerstone of modern medicinal chemistry, enabling the efficient identification of chemically tractable lead candidates from large molecular libraries. In this study, a pharmacophore-based virtual screening strategy was employed to identify potential CDK9 inhibitors from the Zinc database comprising 11719 compounds. A validated ADHRR pharmacophore model was used as the primary screening filter. Application of this model resulted in the identification of 1,641 compounds that fully satisfied all five pharmacophoric constraints (**Figure 7**). The strict feature-mapping criteria ensured high selectivity toward ligands with optimal spatial and functional complementarity to the CDK9 active site. The resulting hit set is chemically diverse and enriched with scaffolds possessing a high likelihood of CDK9 inhibitory activity, thereby providing a robust foundation for further structure-based refinement and experimental validation.

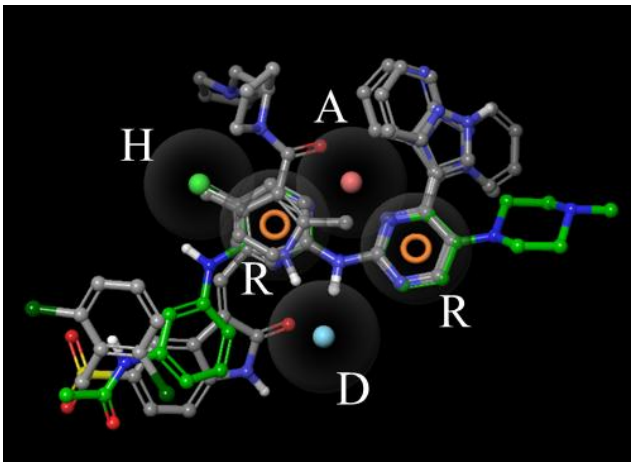


Figure 7. Alignment of resulted hits (grey in color) and most potent compound **23** (green in color).

3.5 Molecular docking-based virtual screening

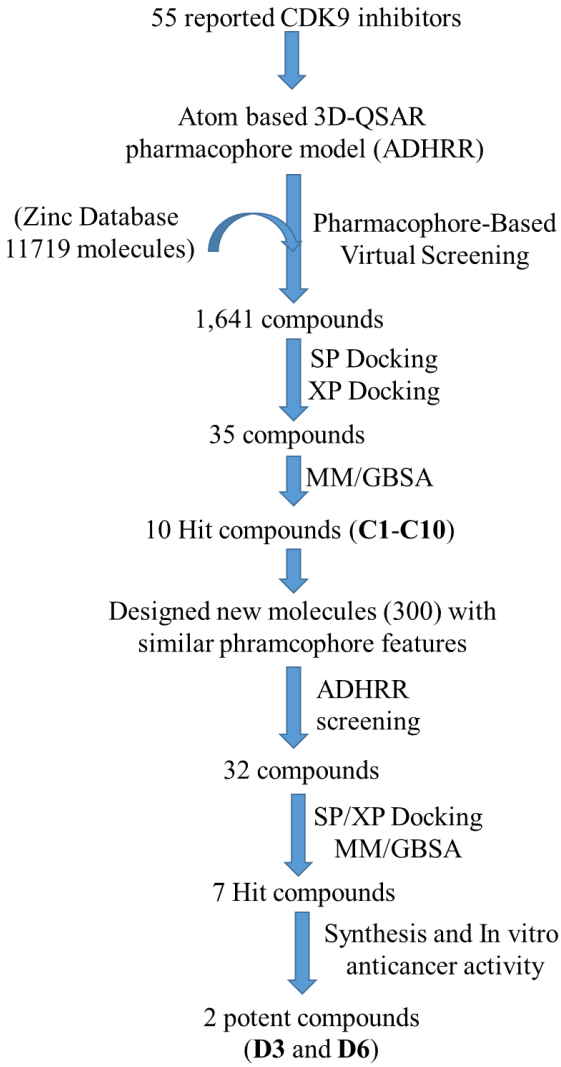


Figure 8. Workflow chart for identification of hit molecules.

Molecular docking studies were subsequently conducted on the pharmacophore-derived hit set to evaluate their binding modes and affinities within the CDK9 active site. Docking simulations were performed using a hierarchical protocol comprising Standard Precision (SP) followed by Extra Precision (XP) docking. Initially, all 1,641 hits obtained from PHASE screening were subjected to SP docking, from which the top-ranked 2% of compounds (35 molecules) exhibiting favourable docking scores and interaction profiles were advanced to XP docking. This successive filtering strategy enabled stringent discrimination of high-affinity binders. From the XP docking results, 10 compounds displaying optimal binding orientations and superior docking scores were selected for binding free energy estimation using Prime MM/GBSA calculations. Figure 8 schematically illustrates the entire virtual screening and selection workflow.

3.6 Interaction studies of screened hits

Ligand-interaction diagram (LID) analysis was performed using the Schrödinger suite to elucidate the key binding interactions of the screened hits within the CDK9 active site. At first, the most potent compound **23** exhibited a well-defined hydrogen-bonding network comprising two interactions, both involving the hinge-region residue Cys106: (i) a hydrogen bond between the pyrimidine ring nitrogen and the backbone of Cys106, and (ii) a hydrogen bond between the pyrimidine -NH group and Cys106, highlighting the importance of the Cys106 residue for stabilization within the CDK9 binding pocket (**Figure 9**). Similarly, the top-ranking hits (**C1-C10**), selected on the basis of favorable MM/GBSA binding free energies, consistently formed one or more hydrogen-bonding interactions with key active-site residues (**Figure 10**). Compound **C2**, which exhibited a binding free energy of -81.72 kcal/mol, formed multiple hydrogen-bonding interactions, including a hydrogen bond between the pyrimidine ring nitrogen and Cys106, as well as hydrogen bonds involving the amine –NH of the pyrimidine and the pyridine ring nitrogen with Cys106 and Lys48, respectively. In addition, a prominent π–π stacking interaction with Phe103 was observed. Similarly, compound **C6** displayed a binding mode comparable to that of compound **23**, characterized by two hydrogen-bonding interactions with Cys106, thereby underscoring the critical role of this residue as an anchoring hotspot for high-affinity CDK9 inhibition.

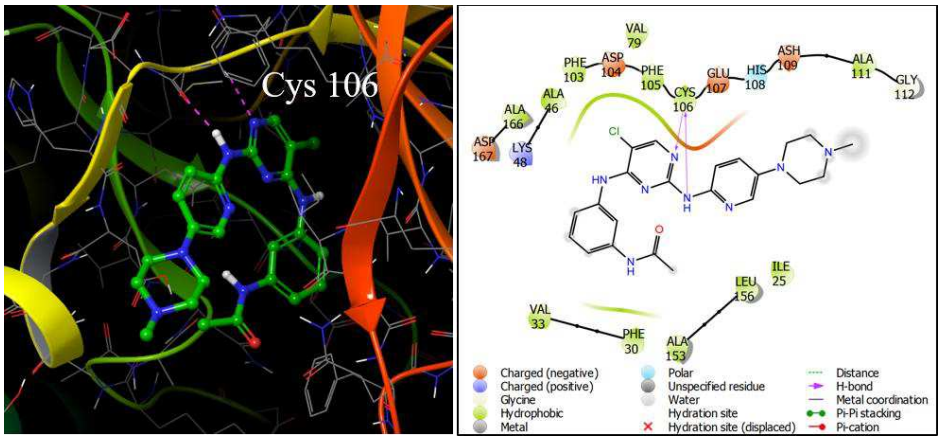


Figure 9. Ligand interaction diagrams (2D&3D) of the most potent compound **23**.

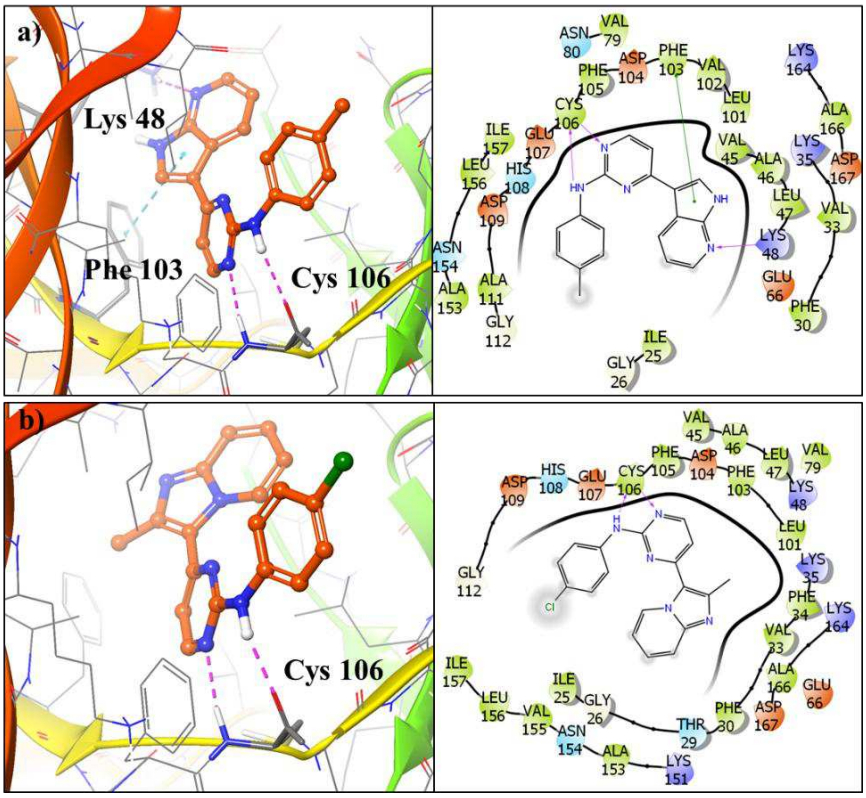
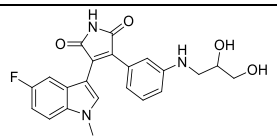
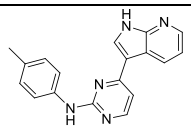
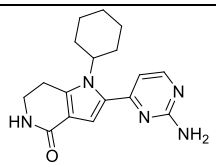
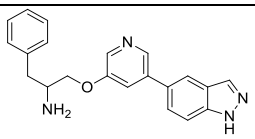
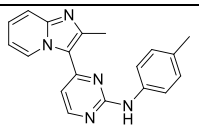
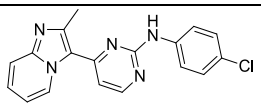
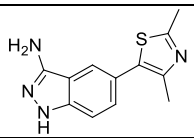
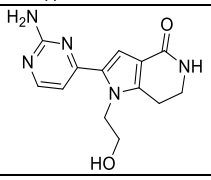
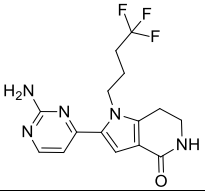
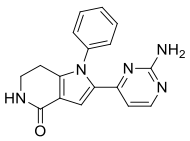


Figure 10. Ligand interaction diagrams (2D&3D) of the top ranking hit molecules **C2** (a) and **C6** (b).

3.7 Binding free energy calculation

The prime MM/GBSA binding free energies of the screened hit molecules are summarized in **Table 2**. As evident from the data, all selected hits exhibited favourable binding free energies when compared with the reference active compound **23**. Notably, compounds **C1-C10** displayed binding free energy values of -75.16, -81.72, -70.01, -75.16, -85.55, -82.73, -75.81, -75.39, -70.50, and -74.38 kcal/mol, which are comparable to or more favourable than that of compound **23**. Cumulatively, these results indicate that the identified hits possess strong predicted binding affinities toward CDK9 and represent promising candidates for further experimental validation.

Table 2. Binding free energies, predicted pIC_{50}, docking score and binding interactions of screened hits (**C1-C10**).

S.No	Com	Structure	Pred. pIC_{50}	Fitness Score	Binding energy (Kcal/mol)	Docking score (Kcal/mol)	Interactions
1.	**C1**		8.441	2.163	-75.16	-10.600	Asn 154 (H-bond), Cys 106 (H-bond), and Asp 104 (H-bond)
2	**C2**		8.550	2.286	-81.72	-9.992	Cys 106 (2*H-bond), Phe 103 (pi-pi) and Lys 48 (H-bond)
3	**C3**		8.097	2.099	-70.01	-9.546	Asp 167 (H-bond), Cys 106 (2*H-bond), and Lys 48 (H-bond)
4	**C4**		8.408	2.030	-75.16	-9.536	Asp 167 (H-bond), Lys 151 (H-bond), Cys 106 (H-bond), and Lys 48 (H-bond)
5	**C5**		8.404	2.313	-85.55	-9.393	Cys 106 (2*H-bond)
6	**C6**		8.573	2.327	-82.73	-9.382	Cys 106 (2*H-bond)
7	**C7**		8.159	2.004	-75.81	-9.324	Cys 106 (H-bond), Asp 104 (H-bond) and Lys 48 (H-bond)
8	**C8**		8.309	2.136	-75.39	-9.045	Cys 106 (H-bond), Asp 104 (H-bond), Lys 48 (H-bond) and Ile 25 (H-bond)
9	**C9**		8.095	2.049	-70.50	-8.995	Cys 106 (2*H-bond) and Lys 48 (H-bond)
10	**C10**		8.120	2.153	-74.38	-8.864	Asp 167 (H-bond) and Cys 106 (2*H-bond)

3.8 *In silico* ADME properties

The predicted ADME properties of the resulting hits (**C1-C10**) are summarized in **Table 3**. Lipophilicity, expressed as the octanol-water partition coefficient (QP log Po/w), is a critical determinant of membrane permeability, metabolic stability, and oral absorption, with values exceeding 5 often associated with poor absorption and increased metabolic liability. As shown in **Table 3**, compounds **C1-C10** exhibiting favorable binding affinities largely conform to Lipinski's rule of five, displaying acceptable physicochemical and pharmacokinetic profiles. Topological polar surface area (PSA), a key descriptor linked to intestinal absorption and oral bioavailability, is generally recommended to remain below 140 Å. The predicted PSA values for the selected hits fall within the range of 36.2-132.4 Å, indicating compatibility with efficient oral absorption. In addition, the predicted aqueous solubility values (QP log S) for the hit compounds are within acceptable limits (< 0.5), suggesting adequate solubility and favorable intestinal permeability. The ability of compounds to penetrate the central nervous system was assessed using QP log BB, which estimates blood-brain barrier permeability. The predicted values for the hit molecules lie within the acceptable range **(**-1.5 to 0.2), indicating controlled BBB penetration and a reduced likelihood of undesired CNS-related side effects. Furthermore, QP log Khsa, which estimates human serum albumin binding, along with QPP Caco-2 cell permeability, were found to be within desirable ranges, supporting favorable distribution and intestinal absorption characteristics. Importantly, the predicted human oral absorption values for the screened hits range from 64.7% to 100%, highlighting their strong potential for oral bioavailability.

Table 3. *In silico* ADME predictions of resulted hits (**C1-C10**).

Com	M.Wt	Don-HB[a]	Acp-HB[b]	n rot[c]	QPlog $P_{O/w}$[d]	QP log S[e]	QPP Caco[f]	PSA[g]	QP log BB[h]	Qplog khsa[i]	%HOA[j]	ROF[k]
C1	409.4	4	7.5	6	1.88	-3.6	74.2	132.4	-1.5	0.03	71.4	0
C2	301.3	2	3.5	2	3.34	-4.4	1208.9	56.8	-0.4	0.43	100	0
C3	311.3	3	5	1	2.11	-4.3	211.3	93.7	-1.0	0.26	80.9	0
C4	344.4	3	4.25	7	3.35	-4.1	118.9	75.5	-0.9	0.44	83.7	0
C5	315.3	1	4	2	4.12	-5.3	2336.7	46.8	-0.1	0.59	100	0
C6	334.8	0	3.5	2	4.66	-5.2	3764.4	36.2	0.2	0.58	100	0
C7	244.3	3	3	1	1.86	-3.5	428.5	69.6	-0.6	-0.01	84.9	0
C8	273.2	4	6.7	4	0.27	-2.5	104.7	110.9	-1.4	-0.44	64.7	0
C9	339.3	3	5	4	2.38	-4.2	212.4	91.3	-0.9	0.07	82.5	0
C10	305.3	3	5	1	2.07	-3.8	259.1	92.0	-0.9	0.14	82.2	0

[a]Number of hydrogen bond donors (<5). [b]Number of hydrogen bond acceptors (<10). [c]Number of rotatable bonds (<15). [d]Logarithm of partition coefficient between n-octanol and water (<5). [e]Aqua solubility parameter (**<**0.5). [f]Caco-2 Cell permeability in nm/s (<25 is poor, >500 is high). [g]Polar Surface Area (<140 Å). [h]Blood/Brain partition co-efficient (-3.5 to 1.2). [i]Human serum albumin binding co-efficient (-1.5 to 1.5). [j]Percentage of human oral absorption (<25 is poor, > 80 is high). [k]Rule of five violations (Lipinski).

4. Designing of new indole-based biphenyl amide hybrids (IBA's)

Virtual screening of the Zinc database identified multiple hit compounds exhibiting favourable binding free energies and well-defined interaction patterns within the CDK9 catalytic domain. Among these, compounds **C2**, **C5**, and **C6** displayed superior binding affinities and key molecular interactions comparable to those of the reference inhibitor **23**, indicating a high degree of structural and energetic similarity in CDK9 engagement. Of note, ten hit compounds demonstrated more favourable binding free energy values than the reference compound (> **-** 68.39 kcal/mol), suggesting enhanced stabilization of the ligand-protein complexes. Interaction analysis revealed that all prioritized hits (**C1**-**C10**) formed two to three conserved hydrogen bonds with residues lining the ATP-binding pocket, interactions that are critical for anchoring the ligands within the hinge region and for effective CDK9 inhibition. Pharmacophore elucidation from these active hits yielded a five-feature model (ADHRR), defining the essential molecular determinants for CDK9 binding. A notable structural convergence among the resulting hits was the presence of a pyrrole or fused pyrrole motif, or pyrrole-derived heterocycles often integrated with a hydrophobic benzene ring, underscoring the importance of this heteroaromatic framework in mediating π–π stacking and hydrophobic interactions within the CDK9 active site. These observations highlight the role of fused heteroaromatic systems in achieving optimal complementarity with the kinase binding pocket. Guided by these pharmacophoric and structural insights, three series of novel indole-based derivatives (300) were rationally designed. The indole scaffold, as a fused pyrrole-benzene system, intrinsically satisfies the identified pharmacophore requirements while offering structural versatility for fine-tuning steric and electronic properties. Accordingly, these newly designed indole derivatives are expected to establish enhanced intermolecular interactions and improved binding free energies, thereby representing promising lead candidates for further optimization as CDK9 inhibitors. A total of 300 newly designed indole-based biphenyl amide hybrids (IBAs) were screened against the validated ADHRR pharmacophore model, resulting in the identification of 32 compounds that fully satisfied all five essential pharmacophoric features (**Figure 11)**.

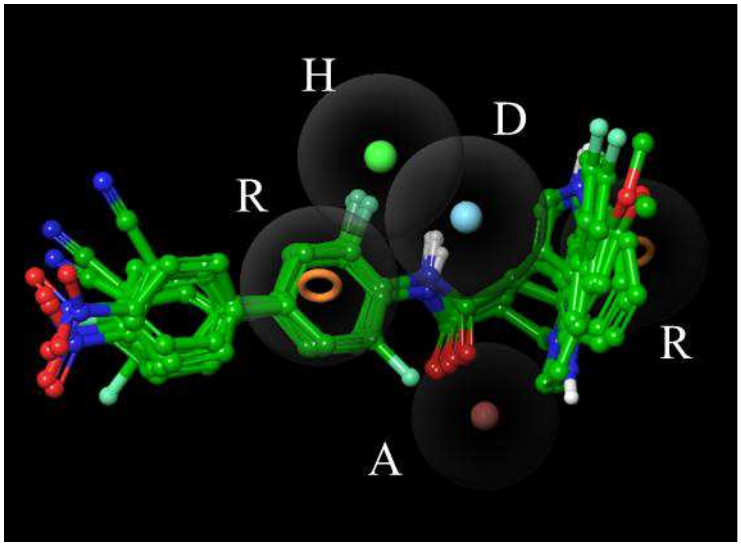


Figure 11. Alignment of IBA's in the ADHRR.

4.1 Molecular docking and binding free energy calculations of IBA's.

These 32 IBAs were later subjected to extra-precision (XP) molecular docking within the CDK9 active site employing the same docking grid and parameters used for the initial dataset, thereby ensuring methodological consistency. The corresponding ligand-protein interaction profiles of the newly designed IBAs are illustrated in **Figure 12**.

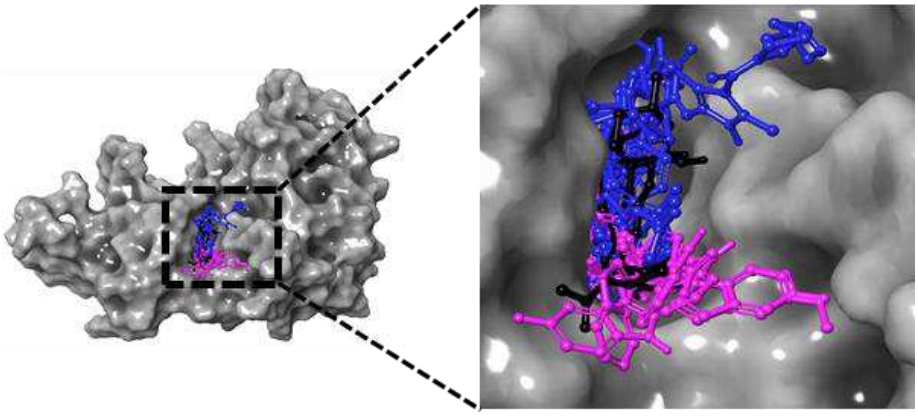


Figure 12. Surface interaction of IBA's (pink), clinical drugs (black) and screened hits from Zinc database (Blue) at ATP binding packet of CDK9.

Interaction analysis revealed that the majority of the designed compounds established conserved hydrogen bonding interactions with Cys106, a key hinge-region residue previously identified as critical for CDK9 inhibition. Importantly, this interaction was also observed in the reference inhibitor **23** as well as in the resulting hits (**C1-C10**) from the Zinc database, exhibiting favourable binding free energy, thereby validating the design strategy. For instance, compound **D3** formed two hydrogen bonds, involving the amide NH with Cys106 and the indole NH with Asp109, respectively. In addition, **D3** exhibited a π-π stacking interaction between its pyridine ring and Phe103 residue, further stabilizing the ligand within the ATP-

binding pocket (**Figure 13**). Similarly, compound **D6**, which demonstrated the most favourable docking score (-9.714 kcal/mol) and binding free energy (-87.55 kcal/mol), formed three key interactions: (i) hydrogen bonding between the amide NH and Cys106, (ii) hydrogen bonding between the cyano nitrogen and Lys48, and (iii) a π–π stacking interaction between the indole ring and His108. These interactions indicate strong and multifaceted engagement with the CDK9 catalytic domain.

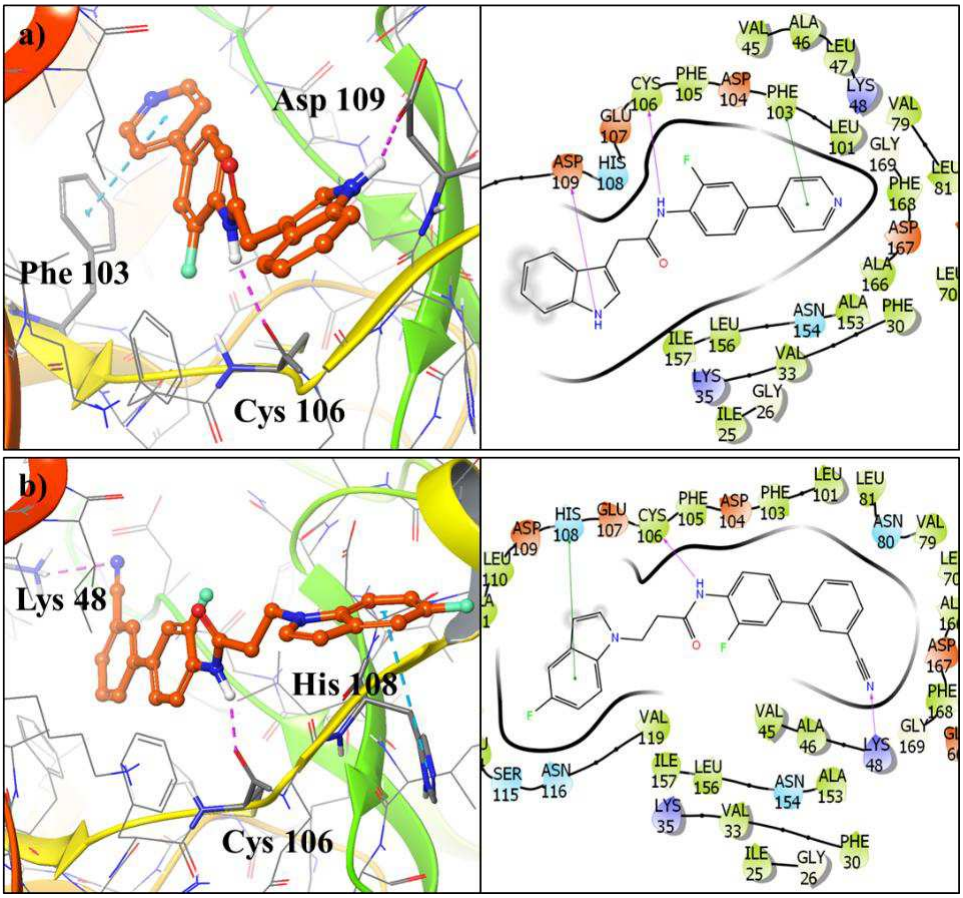
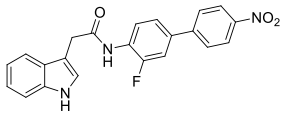
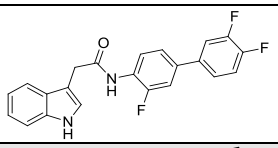
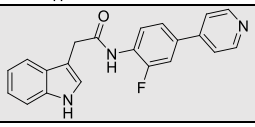
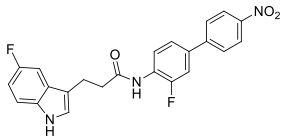
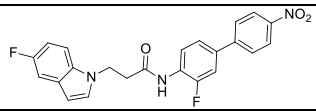
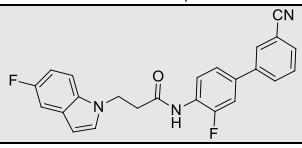
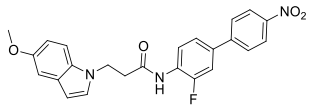


Figure 13. Ligand interaction diagrams: a) **D3**; b) **D6**.

To further validate binding affinity, all docked IBAs were evaluated using Prime MM/GBSA calculations. This analysis identified seven lead compounds (**D1**-**D7**) exhibiting highly favourable binding free energies (**Table 4**), with ΔG_bind values of -70.36, -73.18, -85.33, -79.22, -70.20, -87.55, and -94.05 kcal/mol respectively. Comparative analysis with the reference compound **23** revealed that all seven designed IBA's displayed significantly improved binding free energies, underscoring the effectiveness of the pharmacophore-guided design and confirming their potential as optimized CDK9 inhibitors.

Table 4. Binding free energies, predicted pIC_{50}, docking score and binding interactions of newly designed IBA's (**D1-D7**).

S.No	Com	Structure	Pred. pIC_{50}	Fitness Score	Binding energy (Kcal/mol)	Docking score (Kcal/mol)	Interactions
1	**D1**		8.332	2.394	-70.36	-9.435	Cys 106 (H-bond) and Lys 48, Glu 66 (salt bridges), Asp 167 (H-bond)
2	**D2**		8.493	2.203	-73.18	-9.213	Cys 106 (H-bond)
3	**D3**		8.988	2.973	-85.33	-9.186	Phe 103 (Pi-Pi), (Cys 106 (H-bond) and Asp 109 (H-bond)
4	**D4**		8.150	2.716	-79.22	-9.080	Cys 106 (H-bond), Lys 35 (Pi-cat), and Lys 48, Glu 66 (salt bridges), Asp 167 (H-bond)
5	**D5**		8.461	2.510	-70.20	-8.121	Cys 106 (H-bond)
6	**D6**		9.282	2.632	-87.55	-9.714	Lys 48 (H-bond), Cys 106 (H-bond) and His 108 (Pi-Pi)
7	**D7**		8.895	2.863	-94.05	-9.878	Lys 48, Glu 66 (salt bridges), Asp 167 (H-bond), Cys 106 (H-bond) and His 108 (Pi-Pi)
8	*FVP	-	-	-	-62.438	-9.132	Cys 106 (H-bond) and Ala 153 (H-bond)
9	*RCT	-	-	-	-64.971	-8.539	Cys 106 (2*H-bond) and Ala 153 (H-bond)
10	#AZD	-	-	-	-87.077	-8.748	Cys 106 (2*H-bond) and Lys 35 (H-bond)

*CDK9 inhibitors (FVP: Flavopiridol and RCT: Roscovitine); (**Figures S1: Supplementary Information**). #Co-crystal ligand (AZD: AZD4573).

4.2 *In silico* ADME properties of IBA's

The predicted ADME parameters of the IBA's are summarized in **Table 5**. The IBA's largely conform to Lipinski's rule of five, with acceptable parameters and minor deviations in

lipophilicity (QP log Po/w < 5). Predicted PSA values (48.3-94.8 Å) fall within the optimal range for oral absorption. Aqueous solubility (QP log S < 0.5) supports favorable intestinal permeability. Blood-brain barrier penetration (QP log BB, -1.4 to 0) remained within acceptable limits. Human serum albumin binding and Caco-2 permeability predictions were satisfactory. Importantly, predicted human oral absorption ranged from 86.6 to 100%, indicating strong potential for oral bioavailability.

Table 5. *In silico* ADME predictions of designed molecules (**D1-D7**).

Com	M.Wt	Don-HB[a]	Acp-HB[b]	n rot[c]	QPlog $P_{O/w}$[d]	QP log S[e]	QPP Caco[f]	PSA[g]	QP log BB[h]	Qplog Khsa[i]	%H OA[j]	ROF[k]
D1	389.3	2	3.5	5	4.57	-6.5	284.3	93.4	-1.3	0.8	100	0
D2	380.3	2	2.5	4	5.70	-7.0	2383.7	48.3	0	0.9	100	1
D3	345.3	2	4	4	4.41	-5.9	1323.6	61.2	-0.5	0.5	100	0
D4	421.4	2	3.5	6	5.18	-7.5	231.9	94.8	-1.4	1.0	86.6	1
D5	421.4	1	3.5	6	5.66	-7.7	434.2	83.0	-1.1	1.1	94.3	1
D6	401.4	1	4	6	5.54	-8.3	807.5	64.3	-0.8	0.9	100	1
D7	433.4	1	4.25	7	5.52	-7.6	423.6	91.3	-1.3	1.1	93.34	1

[a]Number of hydrogen bond donors (<5). [b]Number of hydrogen bond acceptors (<10). [c]Number of rotatable bonds (<15). [d]Logarithm of partition coefficient between n-octanol and water (<5). [e]Aqua solubility parameter (<0.5). [f]Caco-2 Cell permeability in nm/s (<25 is poor, >500 is high). [g]Polar Surface Area (<140 Å). [h]Blood/Brain partition co-efficient (-3.5 to 1.2). [i]Human serum albumin binding co-efficient (-1.5 to 1.5). [j]Percentage of human oral absorption (<25 is poor, > 80 is high). [k]Rule of five violations (Lipinski).

4.3 MD simulation

The molecular dynamic simulations were performed for the protein-ligand complexes i.e compounds **D3** and **D6** with CDK9 (BCF) for a period of 100 ns to analyze their stability. The root mean square deviation (RMSD) revealed that the CDK9 with compound **D6** complex initially deviated, followed by stabilization up to 100 ns. Whereas the CDK9-**D3** complex exhibited higher deviation (RMSD value around 7 Å) ranging from 0.5 to 75 ns, suggesting the greater stability of the **D6** complex (**Figure 14**). The root mean square fluctuation (RMSF) analysis of both **D3** and **D6** complexes indicated minimal fluctuations in the active site residues, corroborated the stable ligand binding within the binding pocket. Furthermore, the radius of gyration (Rg) remained relatively constant throughout the simulation for both complexes, confirming that the protein maintained its compact structural conformation. The solvent accessible surface area (SASA) analysis also showed only minor variations during the simulation period, suggesting no major structural changes in the protein. Hydrogen bond analysis demonstrated that compound **D6** maintained an average of 2-3 hydrogen bonds with

key residues such as Cys 106 and Asp 167 during the simulation, while **D3** formed comparatively fewer stable hydrogen bonds (**Figures S2-S3: Supplementary Information**). Overall, the molecular dynamic simulation results reveal that the compound **D6** forms a more stable protein-ligand complex than **D3**, supporting the docking results and indicating its potential as a promising inhibitor.

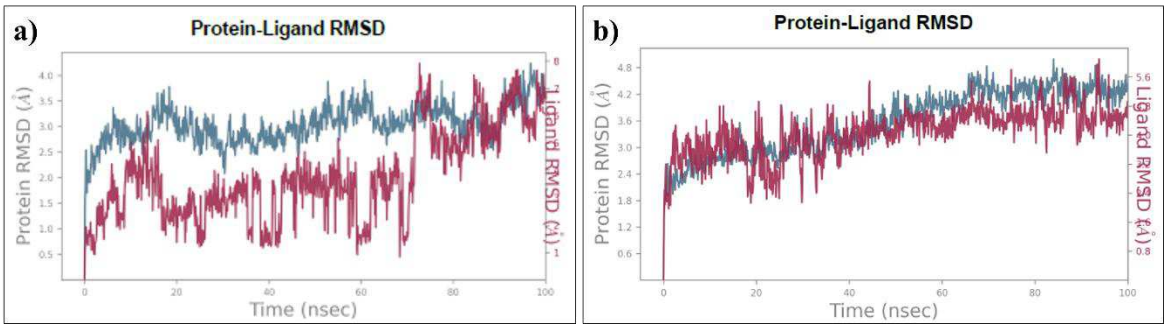


Figure 14. a) RMSD plot of CDK9 + **D3** complex; b) RMSD plot of CDK9 + **D6** complex.

4.4 DFT Analysis of IBA's

Density functional theory (DFT) calculations using the B3LYP functional and 6-31G++(d,p) basis set were performed to optimize the ground-state geometries of the synthesized compounds **D1-D7**. Subsequent HOMO-LUMO analysis provides critical insight into the electronic structure, chemical reactivity, and potential binding behaviour of these molecules toward biological targets. In general, a reduced HOMO-LUMO energy gap (ΔE) is indicative of enhanced chemical reactivity, whereas a wider gap reflects increased kinetic stability. The FMO distributions of the most potent compounds, **D3** and **D6**, are depicted in **Figures 15** and **16**, respectively. In both cases, the HOMO electron density is predominantly localized over the indole moiety in **D3** and **D6**, while the LUMO density is largely centered on the biphenyl rings, suggesting a favourable intramolecular charge-transfer pathway upon excitation or receptor engagement. The calculated HOMO-LUMO energy gaps (ΔE > 6 eV) indicate a balance between electronic stability and controlled reactivity, supporting efficient intermolecular electronic interactions without excessive chemical lability.

Table 6. Electronic parameters of synthesized compounds **D1-D7**.

Com	E_{HOMO} (eV)	E_{LUMO} (eV)	ΔE (eV)	IP (eV)	EA (eV)	η (eV)	σ (eV)	μ (eV)	ω (eV)	χ (eV)
D1	-8.454	-1.480	6.974	8.454	1.480	3.487	0.143	-4.227	2.113	4.967
D2	-8.399	-0.882	7.517	8.399	0.882	3.758	0.133	-4.199	2.009	4.640
D3	-8.278	-0.778	7.500	8.278	0.778	3.75	0.133	-3.75	1.875	4.528
D4	-8.534	-1.536	6.998	8.534	1.536	3.499	0.143	-3.499	1.749	5.035

D5	-8.639	-1.640	6.999	8.639	1.640	3.499	0.143	-3.499	1.749	5.139
D6	-8.523	-1.117	7.406	8.523	1.117	3.703	0.135	-3.703	1.851	4.820
D7	-8.244	1.621	6.623	8.244	1.621	3.311	0.151	-3.311	1.655	4.932

Bandgap (ΔE) = E_{LUMO} - E_{HOMO}, Ionization potential (IP) = - E_{HOMO}, Electron affinity (EA) = - E_{LUMO}, Chemical hardness (η) = (IP-EA)/2, Chemical softness (σ) = 1/(2η), Chemical potential (μ) = - η, Electrophilicity index (ω) = η /2, Electronegativity (χ) = (IP+EA)/2.

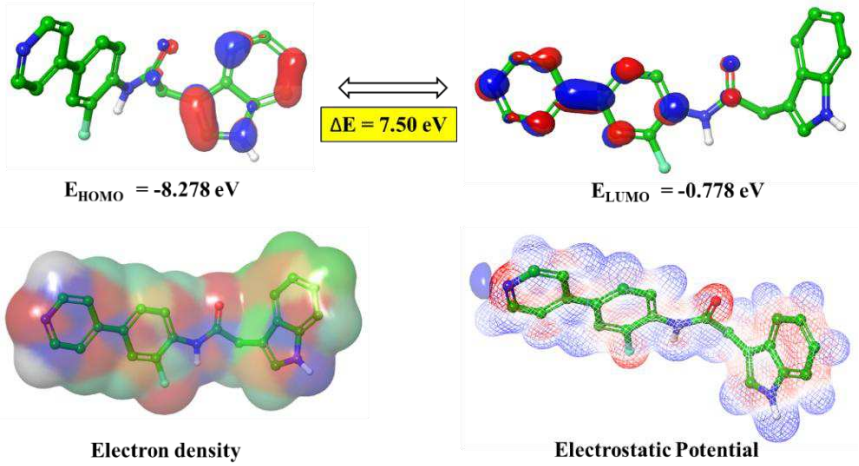


Figure 15. FMO features of **D3**.

To further quantify the electronic characteristics, global reactivity descriptors including electrophilicity index (ω), ionization potential (IP), chemical potential (μ), electron affinity (EA), electronegativity (χ), softness (σ), and chemical hardness (η) were computed for **D1-D7**(**Table 6**). The relatively high electronegativity values (χ = 4.528 eV for **D3** and 4.820 eV for **D6**) reflect strong electron-withdrawing tendencies, while the electrophilicity indices (ω = 1.875 and 1.851 eV, respectively) classify both compounds as strong electrophiles (ω > 1.5 eV). The balanced IP and EA values further suggest an optimal capacity for electron donation and acceptance under physiological conditions. Electrostatic potential (ESP) surface maps reveal well-defined regions of negative and positive electrostatic potential, corresponding to sites susceptible to nucleophilic and electrophilic attack, respectively. Together, the DFT-derived electronic parameters substantiate the chemical stability, favorable charge distribution, and interaction-ready electronic architecture of **D3** and **D6**, reinforcing their suitability as lead candidates for further structure-based optimization.

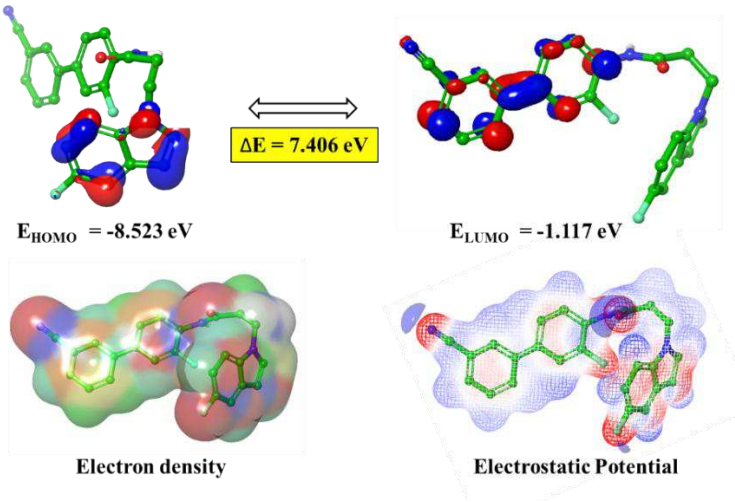
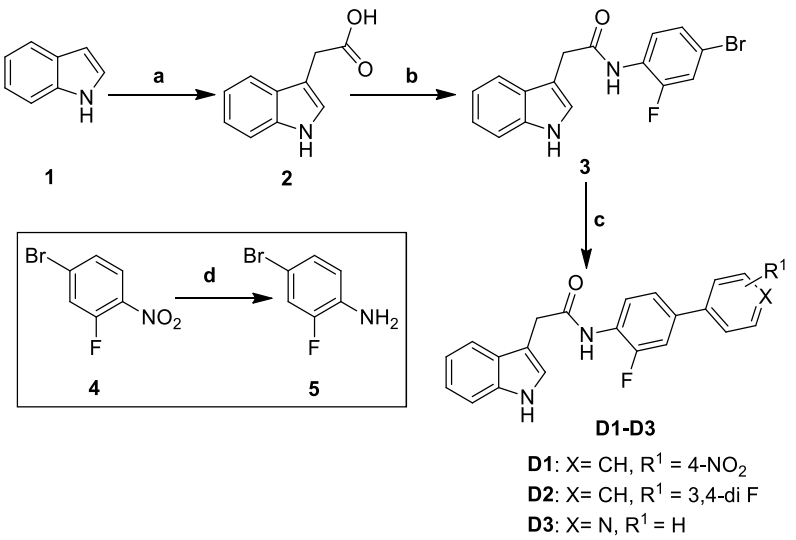


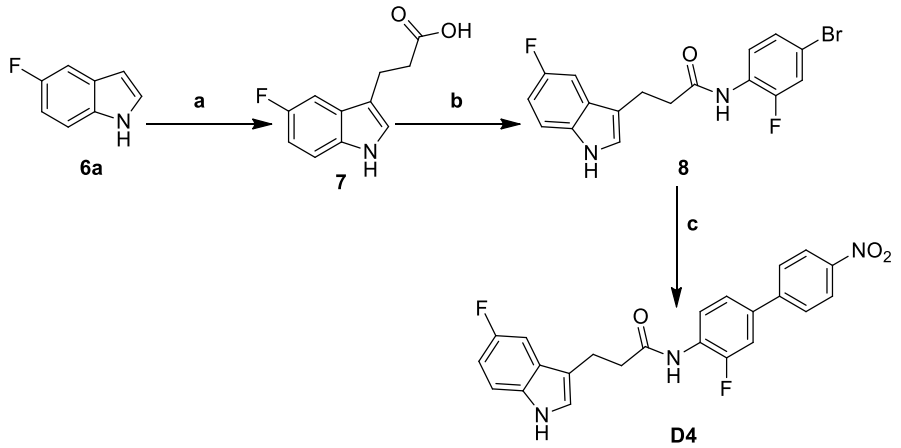
Figure 16. FMO features of **D6**.

4.5 Chemistry of IBA's

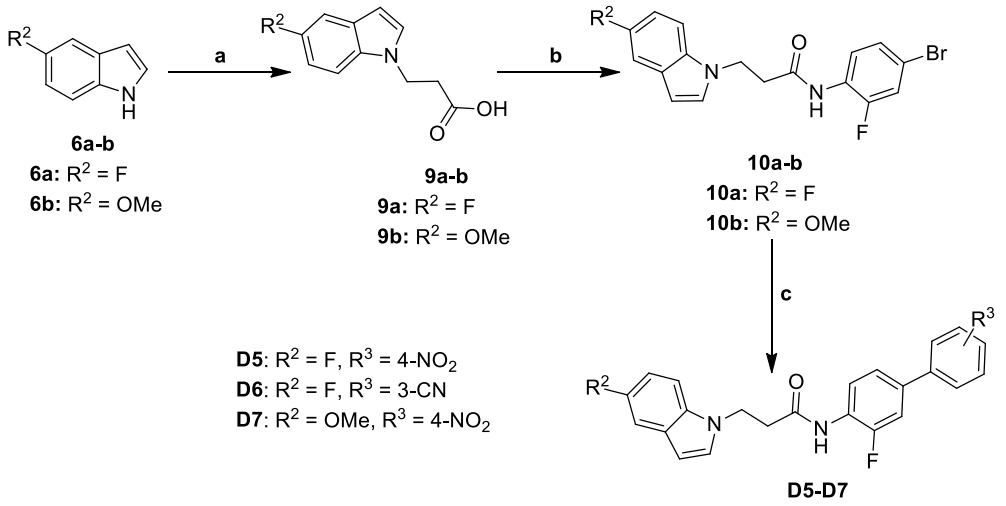
The resulted IBA's from various computational techniques, were synthesized *via* a multi-step protocol, as described in **Schemes 1-3**. Initially, indole-3-acetamide derivatives (**D1-D3**) were synthesized following the strategy outlined in **Scheme 1**. The condensation of indole (**1**) with glycolic acid under basic conditions yielded indole-3-acetic acid (**2**), which was subsequently coupled with amine (**5**) *via* classical HATU-mediated amide bond formation to furnish the key intermediate (**3**). The Suzuki cross-coupling reaction between intermediate (**3**) and the corresponding boronic acids afforded the final compounds (**D1-D3**) in good yields. Next, the synthesis of compound **D4** was accomplished through a sequential approach (**Scheme 2**). The Michael addition of 5-fluoroindole (**6a**) to acrylic acid, generated the corresponding β-keto acid (**7**), which was subjected to amide bond formation with amine (**5**), afforded the brominated intermediate (**8**). Further Suzuki coupling with 4-nitrophenylboronic acid yielded the target compound (**D4**). Finally, *N*-substituted indole derivatives were synthesized following a similar synthetic route (**Scheme 3**). Initially, *N*-alkylation of 5-substituted indoles (**6a-b**) with 3-bromopropanoic acid furnished the carboxylic acid intermediates (**9a-b**), which were coupled with amine (**5**) using HATU-mediated coupling to yield the brominated intermediates (**10a–b**). Suzuki cross-coupling between these brominated intermediates and boronic acids afford the final set of target compounds (**D4-D7**).



Scheme 1. Synthetic protocol for compounds **D1-D3**. Reagents and conditions: a) glycolic acid, KOH, 180 ºC, 16 h; b) **5**, HATU, DiPEA, DMF, 0 °C-RT, 16 h; c) R^1-$B(OH)_2$, $Pd(dppf)Cl_2$, K_3PO_4, 1,4-dioxane, H_2O, 80 °C, 1-4 h; d) Fe, NH_4Cl, $EtOH/H_2O$, 0 ºC-RT, 16 h.



Scheme 2. Synthetic protocol for compound **D4**. Reagents and conditions: a) Acrylic acid, AcOH, Ac_2O, 0-90 °C, 72 h; b) **5**, HATU, DiPEA, DMF, 0 °C-RT, 16 h; c) (4-nitrophenyl)boronic acid, $Pd(dppf)Cl_2$, K_3PO_4, 1,4-dioxane, H_2O, 80 °C, 1-16 h.



Scheme 3. Synthetic protocol for compounds **D5-D7**. Reagents and conditions: a) NaH, 3-bromopropanoic acid, DMF, 0 ºC-RT, 6 h; b) **5**, HATU, DiPEA, DMF, 0 °C-RT, 16 h; c) R^3-$B(OH)_2$, $Pd(dppf)Cl_2$, K_3PO_4, 1,4-dioxane, H_2O, 80 °C, 1-16 h.

All intermediates and final compounds were rigorously characterized, and their structures were unambiguously established using ^{1}H NMR, ^{13}C NMR, HRMS, and elemental analysis, with complete spectral data provided in the Supplementary Information. In the ^{1}H NMR spectra of the acid derivatives (**2**, **7**, and **9a-b**), a diagnostic singlet appearing between 12.39 and 12.09 ppm was observed and assigned to the carboxylic acid proton (-COOH). For the representative target compound **D1**, a well-defined singlet at 10.02 ppm was attributed to the amide proton (-CONH-) linking the indole and biphenyl fragments. The indole–NH proton resonated as a broad singlet at 10.95 ppm, whereas the aromatic protons appeared as multiplets spanning the range of 8.30-6.98 ppm. The methylene protons were clearly identified as a singlet at 3.87 ppm. The ^{13}C NMR spectrum of **D1** further supported the proposed structure, showing two characteristic downfield signals at 170.8 and 155.1 ppm, corresponding to the amide carbonyl carbon and the fluorine-substituted aromatic carbon, respectively. The remaining aromatic carbons resonated between 147.1 and 108.8 ppm, while the methylene carbon was observed at 33.7 ppm. High-resolution mass spectrometric analyses of all synthesized compounds matched closely with the calculated exact masses, confirming their molecular compositions. In addition, elemental analysis (C, H, N, S) values were within acceptable experimental limits, providing further evidence for the high purity and correct formulation of the synthesized scaffolds.

4.6 Synthesis of IBA's

*4.3.1 2-(1H-indol-3-yl)acetic acid (**2**).* An autoclave was charged with 85% potassium hydroxide (14.37 g, 256.08 mmol) and indole (20 g, 170.72 mmol) then added 70% aqueous glycolic acid (15.58 g, 204.86 mmol) dropwise. The reaction mixture kept at 180 °C for 16 hours. After cooling, the crude was diluted with water (100 mL) and acidified with 12 N hydrochloric acid (P^H: 2-3). The obtained solid was washed with cool water, dried under vacuum to afford **2** (16.5 g, 55%) as an off-white solid. ^{1}H NMR (DMSO-d_6, 400 MHz, δ in ppm): 12.16 (s, 1H), 10.91 (s, 1H), 7.51 (d, J = 8.0 Hz, 1H), 7.36 (d, J = 8.0 Hz, 1H), 7.24 (d, J = 2.4 Hz, 1H), 7.08 (t, J = 7.2 Hz, 1H), 6.99 (t, J = 7.2 Hz, 1H), 3.68 (s, 2H); ^{13}C NMR (100 MHz, DMSO-d_6) δ (ppm): 173.7, 136.5, 127.7, 124.5, 124.3, 121.6, 119.1, 111.8, 108.1, 31.4; ESI-MS (*m/z*) = 176.10 $(M+H)^+$; calculated for $C_{10}H_9NO_2$; C, 68.56; H, 5.18; N, 8.00; Found: C, 68.57; H, 5.12; N, 8.02.

*4.3.2 N-(4-bromo-2-fluorophenyl)-2-(1H-indol-3-yl)acetamide (**3**).* A solution of 2-(1*H*-indol-3-yl)acetic acid **2** (15 g, 85.62 mmol) in dry DMF (150 mL) was cooled to 0 °C and stirred, after which HATU (39.04 g, 102.74 mmol) and DiPEA (22.21 g, 171.24 mmol) were added sequentially. To this activated mixture, 4-bromo-2-fluoroaniline 5 (17.54 g, 94.18 mmol) was added portionwise. The reaction was allowed to warm to room temperature and stirred for approximately 16 h. Upon completion, the reaction mixture was diluted with ethyl acetate and extracted (3 × 250 mL). The combined organic layers were dried over anhydrous Na_2SO_4, filtered, and concentrated under reduced pressure. The resulting crude product was purified by silica gel column chromatography using petroleum ether/ethyl acetate (90:10) as the eluent to afford *N*-(4-bromo-2-fluorophenyl)-2-(1*H*-indol-3-yl)acetamide **3** (18.5 g, 63%) as an off-white solid. ^{1}H NMR (400 MHz, $CDCl_3$) δ in ppm: 8.30 (s, 1H), 8.25 (t, J = 8.6 Hz, 1H), 7.68-7.61 (m, 2H), 7.46 (dt, J = 8.1, 1.0 Hz, 1H), 7.34-7.19 (m, 4H), 7.15 (dd, J = 10.3, 2.2 Hz, 1H), 3.95 (d, J = 0.8 Hz, 2H); ^{13}C NMR (100 MHz, $CDCl_3$) δ (ppm): δ 172.3, 155.1, 153.1, 137.4, 128.1, 127.3, 126.8, 126.7, 123.6, 121.6, 120.1, 119.5, 115.6, 111.5, 108.5, 35.4; ESI-MS (*m/z*) = 347.19 $(M+H)^+$; calculated for $C_{16}H_{12}BrFN_2O$; C, 55.35; H, 3.48; N, 8.07; Found: C, 55.31; H, 3.42; N, 8.09.

*4.3.3 General Procedure for synthesis of N-(3-fluoro-[1,1'-biphenyl]-4-yl)-2-(1H-indol-3-yl)acetamide derivatives (**D1-D3**).* A mixture of compound **3** (250 mg, 1.0 mmol) and the appropriate substituted boronic acid (1.0 mmol) was dissolved in a 1,4-dioxane/H_2O solvent system (3:1, v/v) and stirred, followed by the addition of K_3PO_4 (2.0 mmol). The reaction

mixture was degassed by purging with argon for 10-15 min, after which $Pd(dppf)Cl_2$ (0.01 mmol) was added. The resulting mixture was heated at 80 °C and stirred until complete consumption of the starting material, as monitored by TLC. After completion, the reaction mixture was cooled to room temperature, diluted with water, and extracted with ethyl acetate (3 × 25 mL). The combined organic extracts were washed with brine (30 mL), dried over anhydrous Na_2SO_4, filtered, and concentrated under reduced pressure. The crude product was purified by silica gel column chromatography using a petroleum ether/ethyl acetate solvent system to afford the desired compounds **D1**-**D3**.

*4.3.3.1 N-(3-fluoro-4'-nitro-[1,1'-biphenyl]-4-yl)-2-(1H-indol-3-yl)acetamide (**D1**).* Yield: 88%; ^{1}H NMR (DMSO-d_6, 400 MHz, δ in ppm): 10.95 (s, 1H), 10.02 (s, 1H), 8.30 – 8.28 (m, 2H), 8.13 (t, J = 8.4 Hz, 1H), 8.01 – 7.99 (m, 2H), 7.79 (dd, J = 12.4, 2.2 Hz, 1H), 7.65 – 7.62 (m, 2H), 7.37 (dt, J = 8.1, 0.9 Hz, 1H), 7.30 (d, J = 2.4 Hz, 1H), 7.09 (ddd, J = 8.2, 7.0, 1.3 Hz, 1H), 7.00 (ddd, J = 8.0, 6.9, 1.1 Hz, 1H), 3.87 (s, 2H). ^{13}C NMR (100 MHz, DMSO-d_6) δ (ppm) 170.83, 147.14, 145.25, 136.61, 134.49, 128.01, 127.84, 127.73, 127.69, 124.55, 124.51, 124.21, 123.70, 123.67, 121.51, 119.15, 118.92, 114.73, 114.52, 111.87, 108.76, 33.71. ESI-MS: m/z 389.39 $(M+H)^+$; calculated for $C_{22}H_{16}FN_3O_3$; C, 67.86; H, 4.14; N, 10.79; Found: C, 67.81; H, 4.17; N, 10.74.

*4.3.3.2 2-(1H-indol-3-yl)-N-(3,3',4'-trifluoro-[1,1'-biphenyl]-4-yl)acetamide (**D2**).* Yield: 72%; ^{1}H NMR (DMSO-d_6, 400 MHz, δ in ppm): 10.94 (s, 1H), 9.94 (s, 1H), 8.18 (s, 1H), 8.02 (t, J = 8.4 Hz, 1H), 7.83 (ddd, J = 12.4, 7.8, 2.2 Hz, 2H), 7.69 – 7.60 (m, 2H), 7.58 – 7.49 (m, 1H), 7.37 (dq, J = 8.1, 1.3 Hz, 1H), 7.29 (dd, J = 5.6, 2.3 Hz, 1H), 7.15 – 7.06 (m, 1H), 7.02 – 6.97 (m, 1H), 3.85 (s, 2H); ^{13}C NMR (100 MHz, DMSO-d_6) δ (ppm): 170.72, 155.26, 152.82, 148.5, 136.62, 134.96, 127.71, 124.49, 123.65, 122.92, 121.51, 119.16, 118.91, 118.44, 118.27, 116.11, 115.93, 114.18, 113.97, 111.87, 108.84, 33.68; ESI-MS: m/z 380.37 (M+H)+; calculated for $C_{22}H_{15}F_3N_2O$; C, 69.47; H, 3.98; N, 7.36; Found: C, 69.41; H, 3.99; N, 7.38.

*4.3.3.3 N-(2-fluoro-4-(pyridin-4-yl)phenyl)-2-(1H-indol-3-yl)acetamide (**D3**).* Yield: 89%; ^{1}H NMR (DMSO-d_6, 400 MHz, δ in ppm): 10.94 (s, 1H), 10.01 (s, 1H), 8.62 (d, J = 5.4 Hz, 2H), 8.12 (t, J = 8.4 Hz, 1H), 7.86 – 7.71 (m, 3H), 7.71 – 7.60 (m, 2H), 7.44 – 7.33 (m, 1H), 7.30 (d, J = 2.4 Hz, 1H), 7.09 (ddd, J = 8.1, 6.9, 1.3 Hz, 1H), 7.00 (ddd, J = 8.1, 7.0, 1.1 Hz, 1H), 3.87 (s, 2H); ^{13}C NMR (100 MHz, DMSO-d_6) δ (ppm): 170.81, 150.73, 145.68, 136.61, 127.98, 127.86, 127.69, 124.51, 124.21, 123.16, 121.51, 121.29, 119.15, 118.91, 114.27, 114.06,

111.87, 108.76, 33.70; ESI-MS: m/z 345.38 (M+H)+; calculated for $C_{21}H_{16}FN_3O$; C, 73.03; H, 4.67; N, 12.17; Found: C, 73.05; H, 4.66; N, 12.19;

4.3.4 3-(5-fluoro-1H-indol-3-yl)propanoic acid (7). A solution of 5-fluoro-1*H*-indole (15 g, 110.99 mmol) in glacial acetic acid (150 mL) was cooled to 0 °C, and acrylic acid (9.59 g, 113.19 mmol) followed by acetic anhydride (13.59 g, 113.19 mmol) were added slowly with stirring. The reaction mixture was then heated to 130 °C and stirred for approximately 16 h. After completion, the reaction mixture was concentrated to dryness under reduced pressure. The resulting residue was neutralized with aqueous NaOH, and the precipitated solid was removed by filtration. The clear filtrate was subsequently acidified with aqueous HCl and extracted with ethyl acetate (3 × 250 mL). The combined organic layers were dried over anhydrous Na_2SO_4, filtered, and concentrated under reduced pressure. The crude product was purified by silica gel column chromatography using petroleum ether/ethyl acetate (70:30) as the eluent to afford compound **7** (11.5 g, 50%) as an off-white solid. m.p: 114-115 °C; ^{1}H NMR (DMSO-d_6, 400 MHz, δ in ppm): 12.09 (s, 1H), 10.90 (s, 1H), 7.30-7.27 (m, 2H), 7.20 (d, J = 1.6 Hz, 1H), 6.90 (dt, J = 9.2, 2.4 Hz, 1H), 2.90 (t, J = 7.2 Hz, 2H), 2.57 (t, J = 7.2 Hz, 2H); ^{13}C NMR (100 MHz, DMSO-d_6) δ (ppm): 175.0, 158.2, 133.2, 127.5, 124.9, 114.2, 112.8, 109.7, 103.3, 35.0, 20.5; ESI-MS (*m/z*) = 208.43 $(M+H)^+$; calculated for $C_{11}H_{10}FNO_2$; C, 63.76; H, 4.86; N, 6.76; Found: C, 63.86; H, 4.92; N, 6.73.

*4.3.5 3-(5-fluoro-1H-indol-3-yl)-N-(3-fluoro-4'-nitro-[1,1'-biphenyl]-4-yl)propanamide (**D4**).* The similar protocol (synthesis of compounds **D1-D3**) was followed. The obtained crude solid was purified by using column chromatography with pet ether/ethyl acetate system to give compounds **D4**. Yield: 74%; ^{1}H NMR (DMSO-d_6, 400 MHz, δ in ppm): 10.89 (s, 1H), 9.90 (s, 1H), 8.29 (d, J = 6.8 Hz, 2H), 8.17-8.13 (m, 1H), 7.99 (d, J = 7.2 Hz, 2H), 7.76 (dd, J = 10.0, 1.6 Hz, 1H), 7.63 (dd, J = 6.8, 0.8 Hz, 1H), 7.36-7.31 (m, 2H), 7.24 (s, 1H), 6.90 (td, J = 3.6, 2.0 Hz, 1H), 3.00 (t, J = 6.0 Hz, 2H), 2.80 (t, J = 6.0 Hz, 2H); ESI-MS (m/z) = 422.145 $(M+H)^+$; Anal. calcd. for $C_{23}H_{17}F_2N_3O_3$; C, 65.55; H, 4.07; N, 9.97. Found: C, 65.51; H, 4.04; N, 9.96.

*4.3.6 General Procedure for synthesis of N-(4-fluoro-[1,1'-biphenyl]-3-yl)-3-(1H-indol-1-yl)propanamide derivatives (**D5-D7**):* The similar protocol (synthesis of compounds **D1-D3**) was followed. The obtained crude solids were purified by using column chromatography with pet ether/ethyl acetate system to give compounds **D5-D7**.

*4.3.6.1 3-(5-fluoro-1H-indol-1-yl)-N-(3-fluoro-4'-nitro-[1,1'-biphenyl]-3-yl)propenamide (**D5**).* Yield: 81%; ^{1}H NMR (DMSO-d_6, 400 MHz, δ in ppm): 9.98 (s, 1H), 8.32 – 8.24 (m,

2H), 8.09 (q, *J* = 8.3 Hz, 1H), 8.02 – 7.95 (m, 2H), 7.76 (dd, *J* = 12.4, 2.1 Hz, 1H), 7.63 (dd, *J* = 8.5, 2.1 Hz, 1H), 7.56 (dd, *J* = 9.0, 4.5 Hz, 1H), 7.44 (d, *J* = 3.1 Hz, 1H), 7.31 (dd, *J* = 9.9, 2.6 Hz, 1H), 7.01 (td, *J* = 9.2, 2.6 Hz, 1H), 6.42 (d, *J* = 3.1 Hz, 1H), 4.52 (t, *J* = 6.7 Hz, 2H), 2.97 (t, *J* = 6.7 Hz, 2H); ^{13}C NMR (100 MHz, DMSO-d_6) δ (ppm) 170.13, 158.69, 156.39, 147.15, 145.21, 134.74, 132.79, 130.97, 128.84, 128.03, 127.39, 124.56, 124.30, 123.72, 114.78, 111.45, 109.73, 105.53, 101.32, 42.46, 37.17; ESI-MS (m/z) = 421.40 $(M+H)^+$; Anal. calcd. for $C_{23}H_{17}F_2N_3O_3$; C, 65.56; H, 4.07; N, 9.97. Found: C, 65.58; H, 4.01; N, 9.98.

*4.3.6.2 N-(3'-cyano-3-fluoro-[1,1'-biphenyl]-4-yl)-3-(5-fluoro-1H-indol-1-yl)propanamide (**D6**).* Yield: 73%; ^{1}H NMR (DMSO-d_6, 400 MHz, δ in ppm): 9.93 (s, 1H), 8.20 (s, 1H), 8.08 - 7.98 (m, 2H), 7.86–7.79 (m, 1H), 7.76-7.52 (m, 4H), 7.44 (d, *J* = 3.2 Hz, 1H), 7.31 (dd, *J* = 9.9, 2.7 Hz, 1H), 7.01 (qd, *J* = 8.3, 2.6 Hz, 1H), 6.42 (d, *J* = 3.2 Hz, 1H), 4.52 (t, *J* = 6.7 Hz, 2H), 2.96 (t, *J* = 6.8 Hz, 2H); ^{13}C NMR (100 MHz, DMSO-d_6) δ (ppm): 170.05, 156.38, 155.17, 139.91, 135.18, 132.78, 131.69, 130.97, 130.64, 130.52, 129.47, 128.73, 126.65, 124.48, 123.2, 119.21, 114.43, 112.61, 111.44, 109.73, 105.53, 101.32, 42.46, 37.12; ESI-MS (m/z) = 401.42 $(M+H)^+$; Anal. calcd. for $C_{24}H_{17}F_2N_3O$; C, 71.81; H, 4.27; N, 10.47. Found: C, 71.83; H, 4.24; N, 10.48.

*4.3.6.3 N-(3-fluoro-4'-nitro-[1,1'-biphenyl]-3-yl)-3-(5-methoxy-1H-indol-1-yl)propenamide (**D7**).* Yield: 85%; ^{1}H NMR (DMSO-d_6, 400 MHz, δ in ppm): 9.98 (s, 1H), 8.29 (d, *J* = 8.3 Hz, 2H), 8.11 (t, *J* = 8.4 Hz, 1H), 7.99 (d, *J* = 8.4 Hz, 2H), 7.77 (d, *J* = 12.4 Hz, 1H), 7.64 (d, *J* = 8.6 Hz, 1H), 7.44 (d, *J* = 8.9 Hz, 1H), 7.31 (d, *J* = 3.1 Hz, 1H), 7.07 – 7.02 (m, 1H), 6.80 (d, *J* = 8.8 Hz, 1H), 6.33 (d, *J* = 3.1 Hz, 1H), 4.47 (t, *J* = 6.7 Hz, 2H), 3.75 (s, 3H), 2.95 (t, *J* = 6.8 Hz, 2H); ^{13}C NMR (100 MHz, DMSO-d_6) δ (ppm): 170.19, 153.94, 152.57, 147.16, 145.22, 131.28, 129.47, 128.99, 128.04, 124.57, 124.32, 123.72, 123.7, 114.78, 114.57, 111.61, 111.01, 102.61, 100.85, 55.78, 42.33, 37.25; ESI-MS (m/z) = 433.44 $(M+H)^+$; Anal. calcd. for $C_{24}H_{20}FN_3O_4$; C, 66.51; H, 4.65; N, 9.69. Found: C, 66.54; H, 4.66; N, 9.67.

4.7 *In vitro* antiproliferative activity and SAR of IBA's

The anticancer efficacy of the synthesized compounds **D1-D7**, in comparison with the standard drug doxorubicin, was systematically investigated by employing the MTT assay following a 48-hour incubation period. This assessment was carried out against a diverse panel of human cancer cell lines, comprising A549 (lung carcinoma), SiHa and HeLa (cervical carcinoma), as

well as MCF-7 and MDA-MB-231 (breast carcinoma). The resultant data, encapsulated in **Table 7**, are presented as mean ± standard deviation (SD) values.

Table 7. *In vitro* anti-cancer activity (IC_{50} in μM) of synthesized compounds **D1-D7**.

S.no	Comp	A549	SiHa	Hela	MCF-7	MDA-MB -231
1.	**D1**	8.45±0.42	15.42±0.51	13.72±0.71	19.08±0.75	40.22±0.82
2.	**D2**	16.84±1.03	17.26±0.84	6.91±1.08	11.43±0.64	**11.89±1.02**
3.	**D3**	**6.09±1.0**	**3.33±0.84**	7.93±0.62	**9.74±0.5**	19.38±0.64
4.	**D4**	22.74±0.91	10.66±0.77	8.81±0.54	26.42±0.93	>100
5.	**D5**	13.32±0.58	18.71±0.68	12.76±0.37	15.65±1.01	29.76±0.57
6.	**D6**	7.27±1.3	10.36±1.01	**6.64±0.78**	10.82±0.7	22.41±1.1
7.	**D7**	17.36±1.3	5.04±1.20	14.28±1.26	9.84±1.02	27.84±0.3
8.	**Dox.**	4.69±0.72	2.5±0.91	5.8±1.4	8.92±1.27	8.32±0.3

Dox: doxorubicin.

Most of the synthesized compounds demonstrated notable cytotoxic activity against cervical cancer cell lines SiHa and HeLa. Among them, compound **D3** exhibited the most pronounced antiproliferative effect across multiple cancer cell lines, including A549, SiHa, and MCF-7, with IC_{50} values of 6.09 ± 1.0 μM, 3.33 ± 0.84 μM, and 9.74 ± 0.5 μM, respectively. Notably, the strongest cytotoxic response was observed in SiHa cells, indicating a higher sensitivity of this cell line to **D3**. Similarly, compound **D6** demonstrated preferential cytotoxicity toward HeLa cells, exhibiting an IC_{50} of 6.64 ± 0.78 μM, suggesting a degree of cytospecificity for this cervical carcinoma cell line over others tested (**Figure 18a**). Furthermore, compound **D2** selectively inhibited the growth of the triple-negative breast cancer (TNBC) cell line MDA-MB-231, with an IC_{50} of 11.89 ± 1.02 μM, underscoring its potential specificity towards this aggressive breast cancer subtype. To evaluate the general cytotoxicity, compounds D1-D7 were further assessed against the HEK-293t (normal human embryonic kidney) cell line. Tested derivatives exhibited relatively less toxicity profiles, with the IC_{50} values of 54.8 ± 0.43 μM, 66.34 ± 1.7 μM, 68.79 ± 0.8 μM, 49.25 ± 0.4 μM, 54.18 ± 0.23 μM, 60.41 ± 0.37 μM, and 57.34 ± 0.93 μM, respectively (**Table 8**). Among them, the most potent analogues, **D3** and **D6**, demonstrated minimal inhibitory effects on HEK-293t cells, reflecting a high degree of cytospecificity towards SiHa and HeLa cells. The selectivity index (SI) analysis further substantiated the preferential cytotoxicity of D3 and D6 toward malignant cells (**Figure 18b**). Interestingly, compound D6 demonstrated improved selectivity toward the majority of cancer

cell lines, except against the triple-negative breast cancer cell line (MDA-MB-231). The selectivity hierarchy for **D3** was ranked as follows: SiHa > A549 > HeLa > MCF-7 > MDA-MB-231. Conversely, for compound **D6**, the selectivity order was: HeLa > A549 > SiHa > MCF-7 > MDA-MB-231.

Table 8. Toxicity (IC_{50} in µM) and Selective index (SI) **D1-D7** against normal cell line HEK-293t.

			Selective index (SI)				
S.No	**Comp**	**HEK-293t**	**A549**	**SiHa**	**Hela**	**MCF-7**	**MDA-MB-231**
1.	**D1**	54.8±0.43	6.5	3.5	4.0	2.9	1.4
2.	**D2**	66.34±1.7	3.9	3.8	9.6	5.8	5.7
3.	**D3**	68.79±0.8	11.3	20.6	8.7	7.1	6.6
4.	**D4**	49.25±0.4	2.1	4.6	7.2	1.9	<0.5
5.	**D5**	54.18±0.23	4.1	2.9	4.2	3.5	1.8
6.	**D6**	60.41±0.37	8.3	5.8	9.1	5.6	2.7
7.	**D7**	57.34±0.93	3.3	11.4	4.0	5.8	2.0

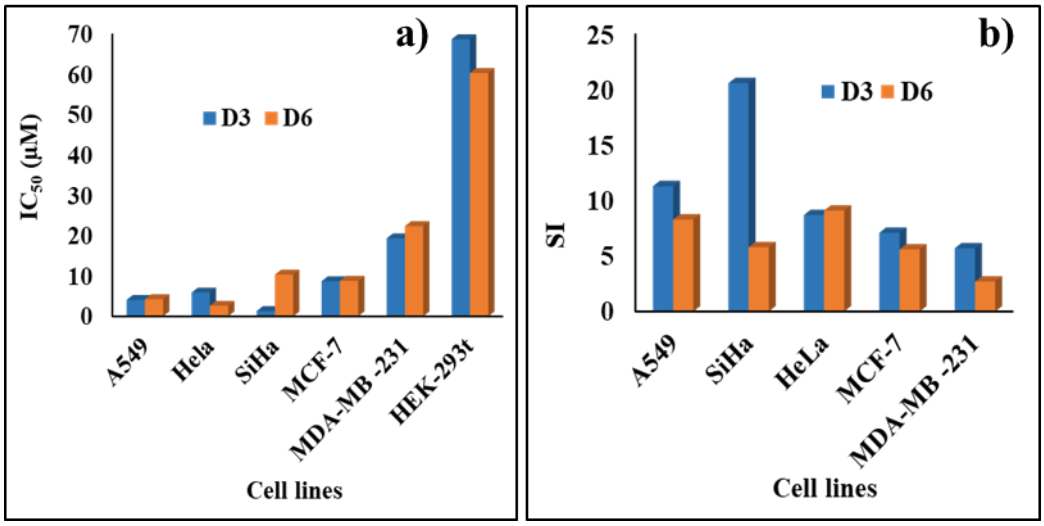


Figure 18. Cytospecificity and Selectivity index (SI) of **D3** and **D6**.

4.8 Comparative study

In comparison, compound **23** emerged as the most promising compound, exhibiting the highest predicted inhibitory potency (Pred. pIC_{50} : 10.17), thereby highlighting its strong compatibility with the selected pharmacophore hypothesis. The calculated MM/GBSA binding free energy of -68.39 Kcal/mol suggests a favourable and energetically stable interaction within the CDK9 binding pocket. Compound **23** established key interactions with the catalytically relevant

residue Cys106 at the hinge region, a critical determinant of CDK9 inhibition, which plausibly accounts for its superior experimental potency (Expt. pIC_{50}: 10.40). Encouragingly, the newly identified indole-based biphenyl amide hybrids (IBA's) **D1-D7** displayed improved binding free energies and predicted pIC_{50} values relative to compound **23**, while maintaining analogous interactions with essential active-site residues. Among these, compounds **D3** and **D6** are distinguished by forming a hydrogen bond with key residue Cys106, resulting in a high docking score (-9.186 kcal/mol for **D3** and -9.714 kcal/mol for **D6**), a markedly enhanced binding free energy (-85.33 kcal/mol for **D3** and -87.55 kcal/mol for **D6**), and as well the highest predicted pIC_{50} (8.988 for **D3** and 9.282 for **D6**) within the series (**Figure 19**). Consistent with these computational insights, **D3** and **D6** demonstrated the most pronounced *in vitro* antiproliferative activity across multiple cancer cell lines tested, while exerting minimal cytotoxicity toward normal HEK-293T cells, thereby reflecting a favourable therapeutic window. Overall, these integrated computational and biological data highlight **D3 and D6** as highly promising CDK9 inhibitory scaffolds; however, definitive elucidation of its inhibitory mechanism and target selectivity necessitates further validation through comprehensive biochemical and mechanistic CDK9 cellular investigations.

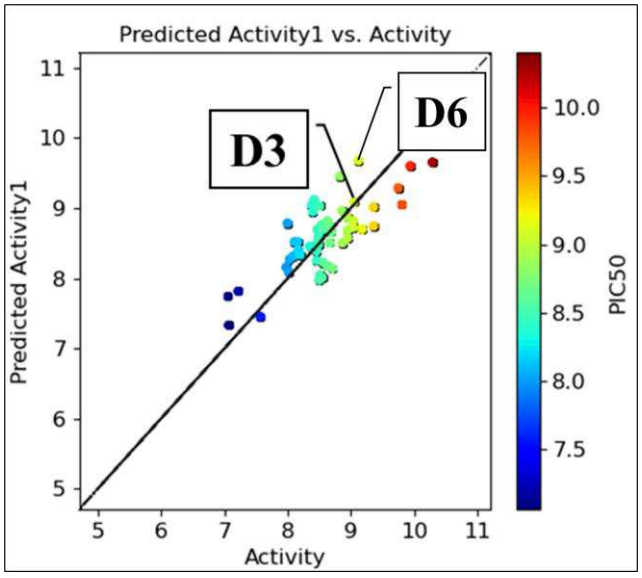


Figure 19. The predicted pIC_{50} of **D3** in the scattered plot.

5. Conclusion

In conclusion, a comprehensive pharmacophore-based virtual screening strategy was employed to identify novel and potent CDK9 inhibitors. The optimized five-point pharmacophore model, ADHRR, was developed using a curated dataset of 55 structurally diverse CDK9 inhibitors and systematically applied to screen the Zinc database. The robustness and predictive reliability of the generated hypothesis were validated using standard statistical protocols, yielding a high

correlation coefficient (R^2 = 0.98). Pharmacophore-matched hits were further subjected to molecular docking within the CDK9 active site, followed by Prime MM/GBSA binding free energy calculations to refine hit selection. From an initial pool of screened hits, ten compounds (**C1**-**C10**) exhibiting favourable pharmacophoric alignment and binding profiles were identified as potential CDK9 inhibitors. Guided by insights derived from the optimized pharmacophore hypothesis, a focused library of indole-based biphenyl amide hybrids (IBA's) was rationally designed and evaluated through ADHRR, molecular docking and binding free energy analysis. Among these, seven compounds (**D1**-**D7**) demonstrated significantly improved binding free energies (-70.20 to -94.05 kcal/mol) compared with the reference active compound **23** (-68.39 kcal/mol). It is evident that most of the newly designed compounds established key hydrogen-bond interactions with Cys106, a critical residue implicated in CDK9 inhibition. MD simulation results supported the docking findings, indicating that the lead compounds **D3** and **D6** form stable complexes with the target protein. Additionally, DFT analysis supported the electronic stability and favourable reactivity profiles of the IBA's. Follow-up chemical synthesis and *in vitro* antiproliferative evaluation revealed that compounds **D3** and **D6** exhibited pronounced cytotoxicity against malignant cell lines while displaying minimal toxicity toward normal human embryonic kidney cells (HEK-293t), indicating a favourable therapeutic index. *In silico* ADME profiling further suggests that all the resulting compounds possess promising oral bioavailability and acceptable pharmacokinetic characteristics. Taken together, the integrated computational experimental workflow combining pharmacophore-based virtual screening, molecular docking, MM/GBSA free energy calculations, ADME prediction, and DFT analysis demonstrates a robust and effective strategy for the discovery of novel CDK9 inhibitors. The lead compounds **D3** and **D6** emerge as particularly promising candidates and warrant further biochemical validation using *in vitro* CDK9 assays and advanced mechanistic studies.

Acknowledgements

The authors are thankful to School of Sciences, Woxsen University and Osmania University for providing the necessary support to conduct the research.

Funding

No funding was received to carry out the present work.

Competing interests

The authors declare no competing interests.

Data Availability

The data that support the findings of this study are available from the corresponding author upon reasonable request.

References

[1] M. Malumbres, M. Barbacid, Cell cycle, CDKs and cancer: a changing paradigm, Nature Reviews Cancer 9 (2009) 153–166.

[2] D.G. Johnson, C.L. Walker, Cyclins and cell cycle checkpoints, Annual Review of Pharmacology and Toxicology 39 (1999) 295–312.

[3] S. Lim, P. Kaldis, Cdks, cyclins and CKIs: roles beyond cell cycle regulation, Development 140 (2013) 3079–3093.

[4] S. Boffo, A. Damato, L. Alfano, A. Giordano, CDK9 inhibitors in acute myeloid leukemia, Journal of Experimental & Clinical Cancer Research 37 (2018) 36.

[5] G. Napolitano, B. Majello, P. Licciardo, A. Giordano, L. Lania, Transcriptional activity of positive transcription elongation factor b kinase in vivo requires the C-terminal domain of RNA polymerase II, Gene 254 (2000) 139–145.

[6] Y.A. Sonawane, M.A. Taylor, J.V. Napoleon, S. Rana, J.I. Contreras, A. Natarajan, Cyclin dependent kinase 9 inhibitors for cancer therapy: miniperspective, Journal of Medicinal Chemistry 59 (2016) 8667–8684.

[7] L.C. Franco, F. Morales, S. Boffo, A. Giordano, CDK9: A key player in cancer and other diseases, Journal of Cellular Biochemistry 119 (2018) 1273–1284.

[8] X. Han, N. Song, A. Saidahmatov, P. Wang, Y. Wang, X. Hu, W. Kan, W. Zhu, L. Gao, M. Zeng, Rational design and development of novel CDK9 inhibitors for the treatment of acute myeloid leukemia, Journal of Medicinal Chemistry 64 (2021) 14647–14663.

[9] B. Barlaam, C. De Savi, A. Dishington, L. Drew, A.D. Ferguson, D. Ferguson, C. Gu, S. Hande, L. Hassall, J. Hawkins, Discovery of a series of 7-azaindoles as potent and highly selective CDK9 inhibitors for transient target engagement, Journal of Medicinal Chemistry 64 (2021) 15189–15213.

[10] B. Barlaam, R. Casella, J. Cidado, C. Cook, C. De Savi, A. Dishington, C.S. Donald, L. Drew, A.D. Ferguson, D. Ferguson, Discovery of AZD4573, a potent and selective inhibitor of CDK9 that enables short duration of target engagement for the treatment of hematological malignancies, Journal of Medicinal Chemistry 63 (2020) 15564–15590.

[11] T. Wu, Z. Qin, Y. Tian, J. Wang, C. Xu, Z. Li, J. Bian, Recent developments in the biology and medicinal chemistry of CDK9 inhibitors: an update, Journal of Medicinal Chemistry 63 (2020) 13228–13257.

[12] Y. Zhang, L. Shan, W. Tang, Y. Ge, C. Li, J. Zhang, Recent discovery and development of inhibitors that target CDK9 and their therapeutic indications, Journal of Medicinal Chemistry 67 (2024) 5185–5215.

[13] B. Zhang, Y. Li, Y. Lin, T. Wang, L. Chen, J. Cai, T. Ji, P. Diao, Y. Ma, Y. Zhang, Structure-Guided Discovery of Novel N 4-(Substituted Thiazol-2-yl)-N 2-(4-Substituted phenyl) pyrimidine-2, 4-Diamines as Potent CDK2 and CDK9 Dual Inhibitors with High Oral Bioavailability, Journal of Medicinal Chemistry 68 (2025) 1693–1715.

[14] A.S.M. Saikat, K. Al-Khafaji, H. Akter, J.-G. Choi, M. Hasan, S.-S. Lee, Nature-Derived Compounds as Potential Bioactive Leads against CDK9-Induced Cancer: Computational and Network Pharmacology Approaches, Processes 10 (2022) 2512.

[15] L. Piazza, C. Poles, G. Bononi, C. Granchi, M. Di Stefano, G. Poli, A. Giordano, A. Medugno, G.M. Napolitano, T. Tuccinardi, Machine Learning-Based Virtual Screening for the Identification of Novel CDK-9 Inhibitors, Biomolecules 16 (2025) 12.

[16] K. Asamitsu, T. Hirokawa, T. Okamoto, Drug design for cyclin-dependent kinase 9 (CDK9) inhibitors in silico, Biochemistry and Biophysics Reports 42 (2025) 101988.

[17] P. Singh, V. Kumar, T.S. Jung, J.S. Lee, K.W. Lee, J.C. Hong, Uncovering potential CDK9 inhibitors from natural compound databases through docking-based virtual screening and MD simulations, Journal of Molecular Modeling 30 (2024) 267.

[18] Q. Yang, Z. Shen, R. Chen, C. Yao, Z. Pan, D. Wu, X. Dong, Identification of Potent CDK9 Inhibitors with Novel Skeletons via Virtual Screening, Biological Evaluation, and Molecular Dynamics Simulation, ACS Medicinal Chemistry Letters 15 (2024) 1654–1661.

[19] S. Wang, F. Liu, P. Li, J.-N. Wang, Y. Mo, B. Lin, Y. Mei, Potent inhibitors targeting cyclin-dependent kinase 9 discovered via virtual high-throughput screening and absolute binding free energy calculations, Physical Chemistry Chemical Physics 26 (2024) 5377–5386.

[20] A.A. Alsfouk, A. Faris, I. Cacciatore, R. Alnajjar, Development of novel CDK9 and CYP3A4 inhibitors for cancer therapy through field and computational approaches, Frontiers in Chemistry 12 (2024) 1473398.

[21] M. Wu, J. Han, Z. Liu, Y. Zhang, C. Huang, J. Li, Z. Li, Identification of novel CDK 9 inhibitors based on virtual screening, molecular dynamics simulation, and biological evaluation, Life Sciences 258 (2020) 118228.

[22] I. Habib, T.A. Chohan, T.A. Chohan, F. Batool, U. Khurshid, A. Khursheed, A. Raza, M. Ansari, A. Hussain, S. Anwar, Integrated computational approaches for designing potent pyrimidine-based CDK9 inhibitors: 3D-QSAR, docking, and molecular dynamics simulations, Computational Biology and Chemistry 108 (2024) 108003.

[23] Y. Wang, X. Chen, Y. Yan, X. Zhu, M. Liu, X. Liu, Discovery and SARs of 5-Chloro-N 4-phenyl-N 2-(pyridin-2-yl) pyrimidine-2, 4-diamine derivatives as oral available and dual CDK 6 and 9 inhibitors with potent antitumor activity, Journal of Medicinal Chemistry 63 (2020) 3327–3347.

[24] T. Wu, B. Yu, Y. Xu, Z. Du, Z. Zhang, Y. Wang, H. Chen, L. ao Zhang, R. Chen, F. Ma, Discovery of selective and potent macrocyclic CDK9 inhibitors for the treatment of osimertinib-resistant non-small-cell lung cancer, Journal of Medicinal Chemistry 66 (2023) 15340–15361.

[25] Y. Zhong, J. Xu, R. Zhou, L. Tang, S. Ding, Z. Ren, N. Song, B. Hu, H. Yang, Y. Sun, Identification of a novel selective CDK9 inhibitor for the treatment of CRC: design, synthesis, and biological activity evaluation, Journal of Medicinal Chemistry 67 (2024) 4739–4756.

[26] G. Madhavi Sastry, M. Adzhigirey, T. Day, R. Annabhimoju, W. Sherman, Protein and ligand preparation: parameters, protocols, and influence on virtual screening enrichments, Journal of Computer-Aided Molecular Design 27 (2013) 221–234.

[27] D. Rathee, V. Lather, H. Dureja, Pharmacophore modeling and 3D QSAR studies for prediction of matrix metalloproteinases inhibitory activity of hydroxamate derivatives, Biotechnology Research and Innovation 1 (2017) 112–122.

[28] V. Kuchana, V. Kashetti, S.K.R. Peddi, S. Sivan, V. Manga, Integrated computational approach for in silico design of new purinyl pyridine derivatives as B-Raf kinase inhibitors, Journal of Receptors and Signal Transduction 42 (2022) 439–453.

[29] U. Etikyala, R. Reddyrajula, T. Vani, V. Kuchana, U. Dalimba, V. Manga, An in silico approach to identify novel and potential Akt1 (protein kinase B-alpha) inhibitors as anticancer drugs, Molecular Diversity 29 (2025) 1009–1032.

[30] U. Etikyala, R. Reddyrajula, A. Pasha, U. kumar Dalimba, S.C. Pawar, V. Manga, Design, synthesis and molecular docking of 5-fluoro indole derivatives as inhibitors of PI3K/Akt signalling pathway in cervical cancer, Journal of Molecular Structure 1312 (2024) 138569.

[31] R. Reddyrajula, U. Etikyala, V. Manga, U. kumar Dalimba, Discovery of 1, 2, 3-triazole incorporated indole-piperazines as potent antitubercular agents: Design, synthesis, in vitro biological evaluation, molecular docking and ADME studies, Bioorganic & Medicinal Chemistry 98 (2024) 117562.

Author contributions statement

R.R. developed, designed, and synthesized the compounds, and wrote and reviewed the original manuscript. R.R. and V.M. supervised the overall project. U.E. carried out the computational studies. D.P., S.P., S.S.H., and A.K. assisted in manuscript preparation and literature review. U.D. reviewed the compound characterization and spectral analysis. M.M.R. and C.S.K. performed the molecular dynamics simulations.

Supplementary Files

This is a list of supplementary files associated with this preprint. Click to download.

- Supportinginformation.docx